Available online at www.sciencedirect.com

ScienceDirect

Geochimica et Cosmochimica Acta 246 (2019) 363–384

Geochimica et Cosmochimica Acta

www.elsevier.com/locate/gca

Temperature dependence of calcite dissolution kinetics in seawater

John D. Naviaux [a,*], Adam V. Subhas [b], Nick E. Rollins [c], Sijia Dong [c], William M. Berelson [c], Jess F. Adkins [a]

[a] California Institute of Technology, Pasadena, CA 91125, USA
[b] Woods Hole Oceanographic Institution, Woods Hole, MA 02543, USA
[c] University of Southern California, Los Angeles, CA 90089, USA

Received 1 August 2018; accepted in revised form 27 November 2018; Available online 5 December 2018

Abstract

Knowledge of the mechanism of calcite dissolution in seawater is a critical component of our understanding of the changing global carbon budget. Towards this goal, we provide the first measurements of the temperature dependence of seawater calcite dissolution kinetics. We measured the dissolution rates of ^{13}C-labeled calcite in seawater at 5, 12, 21, and 37 °C across the full range of saturation states $\left(0 < \Omega = \frac{[Ca^{2+}][CO_3^{2-}]}{K'_{sp}} < 1\right)$. We show that the dissolution rate is non-linearly dependent on Ω and that the degree of non-linearity both increases with temperature, and changes abruptly at "critical" saturation states (Ω_{crit}). The traditional exponential rate law most often utilized in the oceanographic community, $R = k(1 - \Omega)^n$, requires different fits to k and n depending upon the degree of undersaturation. Though we calculate a similar activation energy to other studies far from equilibrium (25 ± 2 kJ/mol), the exponential rate law could not be used to mechanistically explain our near equilibrium results. We turn to an alternative framework, derived from crystal nucleation theory, and find that our results are consistent with calcite dissolution kinetics in seawater being set by the retreat of pre-existing edges/steps from Ω = 1–0.9, defect-assisted etch pit formation from Ω = 0.9–0.75, and finally homogenous etch pit formation from Ω = 0.75–0. The Ω_{crit}s for each mechanism are shifted significantly closer to equilibrium than they occur in dilute solutions, such that ocean acidification may cause marine carbonates to enter faster dissolution regimes more readily than would be expected from previous studies. We use the observed temperature dependence for each dissolution mechanism to calculate step kinetic coefficients (β, cm/s), densities of active nucleation sites (n_s, sites/m^2), and step edge free energies (α, mJ/m^2). Homogenous dissolution is well explained within the surface nucleation framework, but defect-assisted dissolution is not. Dissolution is initiated via step-propagation at all temperatures, but the defect-assisted mechanism is skipped over at 5 °C, potentially due to a lack of nucleation sites. The surface nucleation framework enhances our understanding of calcite dissolution in seawater, but our results suggest that a complete theory will also need to incorporate the role of solution/surface speciation and complexation.

Keywords: Calcite; Carbonate; Dissolution; Kinetics; Seawater; Temperature; Activation energy; Surface; Saturation state; Mechanism

1. INTRODUCTION

Calcium carbonates are among the most abundant and reactive minerals on Earth, and they are an integral part of the ocean alkalinity cycle (Morse and Mackenzie, 1990). The steady state ocean alkalinity balance is set by input from terrestrial weathering and output from carbonate burial in sediments. Marine calcifiers currently produce approximately four times as much carbonate as is buried in sediments, meaning that 3/4 of the mineral carbonate produced must dissolve in the sediment or water column

* Corresponding author.
E-mail address: jnaviaux@caltech.edu (J.D. Naviaux).

https://doi.org/10.1016/j.gca.2018.11.037
0016-7037/

(Milliman et al., 1999; Morse et al., 2007). The geologic record of marine carbonates is often used to make inferences about past climates, but it is difficult to constrain changes in the production of carbonate alkalinity versus burial without knowledge of dissolution kinetics (Archer, 1991; Boudreau and Luo, 2017). Modeling the present and future ocean depends on knowledge of carbonate dissolution kinetic formulations.

Carbonate dissolution has been extensively studied for decades, but the functional form of its kinetic rate law is still debated. The simplest formulation, and the one used most frequently in the oceanographic community, is based upon an assumption that calcite dissolves via attack of water at the surface:

$$CaCO_3 + H_2O \rightleftharpoons Ca^{2+} + CO_3^{2-} + H_2O \quad (1)$$

In transition state theory, the overall dissolution rate (R_{diss}) is the sum of simultaneous forward (R_f) and back (R_b) reactions, each with their own rate constants (k_f, k_b) such that:

$$R_{diss} = R_f - R_b = k_f - k_b[Ca^{2+}]^m[CO_3^{2-}]^m \quad (2a)$$

Here, m is a constant describing the stoichiometry of the dissolution reaction. The forward rate depends solely on k_f in this formulation, as the activity of the solid is assumed to be 1. Substituting in the definitions of $\frac{k_f}{k_b} = [Ca^{2+}]^m[CO_3^{2-}]^m = K_{sp}^m$ and $\Omega = \frac{[Ca^{2+}][CO_3^{2-}]}{K_{sp}}$ yields (Lasaga, 1998):

$$R_{diss} = k_b K_{sp}^m - k_b[Ca^{2+}]^m[CO_3^{2-}]^m = k(1-\Omega^m) \quad (2b)$$

Here, k is the net dissolution rate constant per unit area and $1-\Omega^m$ is a measure of the thermodynamic driving force of the solution. Absent of mechanistic understanding, the oceanographic community has historically fit dissolution rates using the empirical equation (Berner and Morse, 1974; Morse, 1978; Keir, 1980):

$$R_{diss} = k(1-\Omega)^n \quad (2c)$$

Here, n is referred to as the reaction order.

There is an ongoing conversation in the oceanographic community about whether calcite dissolution in natural waters obeys linear kinetics ($m = n = 1$), or if a higher order n is required. The answer has important mechanistic implications, as values of n other than 1 imply that reactions beyond Eq. (1) set the dissolution rate of calcite in the ocean. Linear kinetics may be a reasonable approximation for synthetic calcite in non-seawater solutions (Svensson and Dreybrodt, 1992) far from equilibrium ($\Omega < 0.8$, Cubillas et al., 2005) or with packed calcite beds (Boudreau, 2013; Sulpis et al., 2017), but results with suspended particles both in the laboratory (Morse and Berner, 1972; Keir, 1980, 1983; Walter and Morse, 1985; Teng, 2004; Gehlen et al., 2005; Xu et al., 2012; Subhas et al., 2015) and *in-situ* (Peterson, 1966; Honjo and Erez, 1978; Berelson et al., 1994, 2007; Fukuhara et al., 2008) have consistently reported non-linear relationships between dissolution rate and undersaturation. The discrepancy cannot be attributed solely to uncertainties in calcite's apparent solubility product (Hales and Emerson, 1997), as recent work using updated K_{sp} values has confirmed non-linear kinetics for synthetic (Subhas et al., 2015, 2017; Dong et al., 2018) and biogenic (Subhas et al., 2018) calcites at the near equilibrium undersaturations ($0.7 < \Omega < 1$) most relevant to the modern ocean water column (Olsen et al., 2016).

The oceanographic community has focused on the $(1-\Omega)^n$ rate law, but alternative theories dating back to Burton and Cabrera (1949; Burton et al., 1951; Cabrera and Levine, 1956) argue that the solution driving-force is a necessary, yet ultimately insufficient predictor of reaction kinetics. Crystals are made up of heterogeneous distributions of steps, kinks, defects, and dislocations, and their differing reactivities constrain both the rates and mechanisms of growth/dissolution. For example, it has been shown, using atomic force microscopy (AFM), that calcite dissolution in dilute solutions is limited to pre-existing steps until critical Ω thresholds are surpassed, at which point the overall rate increases dramatically as edge and screw dislocations open to become etch pits (Teng, 2004 and references therein). Models based upon the observed spread of 2D etch pits (Dove et al., 2005, 2008) or pulsing stepwaves (Lasaga and Lüttge, 2001; Lüttge, 2006; Fischer and Lüttge, 2018) allow for these mechanistic transitions and have been used to describe dissolution for a variety of minerals.

The temperature dependence of calcite dissolution kinetics has been extensively studied as a means to understand the mineral's dissolution mechanism, but no study has investigated this dependence in seawater. Knowledge of the elementary reactions and surface complexes responsible for dissolution (Plummer et al., 1978; Busenberg and Plummer, 1986; Chou et al., 1989; Arakaki and Mucci, 1995; Pokrovsky and Schott, 2002), and their respective activation energies (Plummer et al., 1978; Pokrovsky et al., 2009) is limited to simple non-seawater solutions far from equilibrium. It is generally agreed that the dissolution rate of calcite is linearly dependent on the concentration of H^+ for $pH < 4$–5 (Plummer et al., 1978, 1979; Busenberg and Plummer, 1986; Chou et al., 1989; Arakaki and Mucci, 1995; Alkattan et al., 1998), and that the activation energy for the reaction is on the order of 8–10.5 kJ/mol (Sjöberg and Rickard, 1984; Morse and Arvidson, 2002). The dissolution mechanism becomes more complicated at higher pH values as the system enters a regime of mixed transport and surface reaction control (Rickard and Sjöberg, 1983; Sjöberg and Rickard, 1984). Rate constants collected in the mixed control regime combine several processes, so bulk dissolution studies frequently report "apparent," rather than true activation energies. Apparent activation energies vary with solution composition and experimental design, but tend to range from 14 to 25 kJ/mol when measured under atmospheric pCO_2 levels (Sjöberg, 1978; Sjöberg and Rickard, 1984; Gutjahr et al., 1996; Gledhill and Morse, 2006; Finneran and Morse, 2009). Apparent activation energies can reach as high as 60 kJ/mol at elevated pCO_2 (Pokrovsky et al., 2009). AFM studies can calculate activation energies for specific surface processes (MacInnis and Brantley, 1992; Liang et al., 1996; Liang and Baer, 1997; Xu et al., 2010),

but dissolution rates derived from scaling up AFM measurements frequently disagree with those from bulk dissolution measurements (Arvidson et al., 2003; Morse et al., 2007).

The goal of our work is to provide the first measurements of the temperature dependence of calcite dissolution kinetics in seawater. Using the ^{13}C tracer method of Subhas et al. (2015), we dissolve labeled calcite powders in a closed system at 5, 12, 21, and 37 °C across the full range of saturation states. Our experiments are conducted in filtered seawater, and the sensitivity of the ^{13}C tracer method allows us to resolve the near equilibrium Ωs most relevant to the ocean. We gain further insight by applying the surface nucleation model of Dove et al. (2005) to our data to identify changes in dissolution mechanism and to parse the near-equilibrium effects of temperature on the physical and energetic properties of calcite.

2. METHODS

Following the methods of Subhas et al. (2015), ^{13}C labeled calcium carbonate powder was purchased from Sigma Aldrich (SKU 492027, >99 atom%) and wet sieved (solution information below) into 70–100 and 20–53 μm size fractions. The total specific surface areas for each fraction were determined by Kr gas BET to be 900 ± 40 cm^2/g for the 70–100 μm fraction, and 1520 ± 60 cm^2/g for the 20–53 μm fraction. Dissolution rates in the literature are frequently normalized by average geometric surface area (270 and 625 cm^2/g for our samples), but we use BET normalized rates as they produce a tighter agreement between our size fractions. The use of geometric surface area does not affect our results, and for comparison, both geometric surface area rates (g/cm^2/day) and mass normalized rates (g/g/day) are reported alongside our BET surface area rates in the Appendix (Table A1).

It has been shown that a mineral's reaction history can alter densities of steps, edges, and/or etch pits, thereby changing the dissolution rate that is eventually measured (Arvidson et al., 2003; Arvidson and Luttge, 2010; Fischer et al., 2012, 2014). To ensure that our dissolution rates were not an artifact of our choice of sieving liquid, we compared dissolution rates of powders sieved in: (1) pure 18.2 MΩ cm^{-1} water, (2) 18.2 MΩ cm^{-1} water adjusted to pH 8.5 with ammonium hydroxide, and (3) Dickson standard seawater (https://www.nodc.noaa.gov/ocads/oceans/Dickson_CRM/batches.html) adjusted to $\Omega \approx 1$ via HCl addition. A subset of powder that had been sieved in pH 8.5 ammonium hydroxide was also baked at 80 °C under vacuum for 7 days. No differences in subsequent dissolution rates were observed (Fig. S1), so data are reported for powders sieved in 18.2 MΩ cm^{-1} water unless otherwise noted.

Experimental bags were prepared by placing 1–5 mg of $Ca^{13}CO_3$ powder inside a 1-L Supelco bag (part no. 30336-U) that had been modified (Subhas et al., 2015) to include an extra sampling port. The additional ports housed 0.2 μm filters to retain the carbonate powder during sampling. Bags were heat sealed and evacuated to remove all headspace. Experimental fill waters were made separately by first siphoning Dickson standard seawater (Batches 144-165) into another evacuated Supelco bag, and then titrating its total alkalinity (and therefore Ω) to the desired level via injection of 0.1 M HCl. Silicate and phosphate differed between Dickson seawater batches, but only varied between 1–7 and 0.3–0.6 μmol/kg, respectively. Though phosphate adsorbs strongly to calcite surfaces (de Kanel and Morse, 1978; Millero et al., 2001) and is thought to be an inhibitor of dissolution (Berner and Morse, 1974; Sjöberg, 1978), variations in phosphate concentrations did not impact our results. The range of concentrations investigated in this study is much smaller than in studies that have documented significant inhibition (50 μmol/L, Walter and Burton, 1986), and preliminary experiments with seawater spiked to 20 μmol/L phosphate showed no inhibitory effect (not shown).

Each run began by siphoning 50 g of fill water into the experimental bag to pre-rinse the calcite grains and remove any fine particles. The rinse water was subsequently taken out through the sampling port and discarded, after which the bags were filled with ~300 g of seawater and placed in a recirculating water bath set to 5, 12, 21, or 37 °C. The water bath maintained its temperature to ±0.1 °C and was placed on a shaker table set to 85 rpm. No change in dissolution rates were observed at higher shake speeds, but rates dropped significantly when stirring below 60 rpm (Subhas et al., 2015). We used a rate of 85 rpm to ensure that chemical transport was not limiting in our experiments. At no point was any headspace introduced into the system, so there was no change in the dissolved inorganic carbon (DIC) of the water due to exchange with the atmosphere. Fill water was always equilibrated to the desired temperature before being introduced into the experimental bags to ensure that initial measurements were not affected by a gradient in temperature between the bag and the water bath. Although not as important for experiments that ran for several days, this equilibration was crucial in achieving reproducible results in undersaturated waters below $\Omega < 0.5$. Bags were sampled every 6–12 h over the course of 2–5 days.

The samples were analyzed for DIC and ^{13}C using a Picarro cavity ringdown spectrometer. The $\delta^{13}C$ values were converted to moles dissolved per time, with typical traces shown in Fig. 1. The data become linear after an initial equilibration time <24 h (Subhas et al., 2017), and points between 24 and 72 h were fit with a linear regression using Microsoft Excel's Linest function, with the resulting slope taken as the dissolution rate. The relative error on the slope was used as the rate error and typically ranged from 1 to 5%. Total alkalinity was measured by open-system Gran titration and compared against the alkalinity expected from dissolution, as derived from the ^{13}C mass balance. The agreement between these alkalinities was always within 1–4 μmol/kg. The final saturation state was calculated by CO2SYS using measured DIC, total alkalinity, and temperature. Standard errors in DIC (±2–4 μmol/kg) and alkalinity (±1–3 μmol/kg) were propagated using a Monte Carlo approach, giving a final error on Ω of 0.01–0.04 units. We used the carbonate system dissociation constants from the Dickson and Millero (1987) refit to

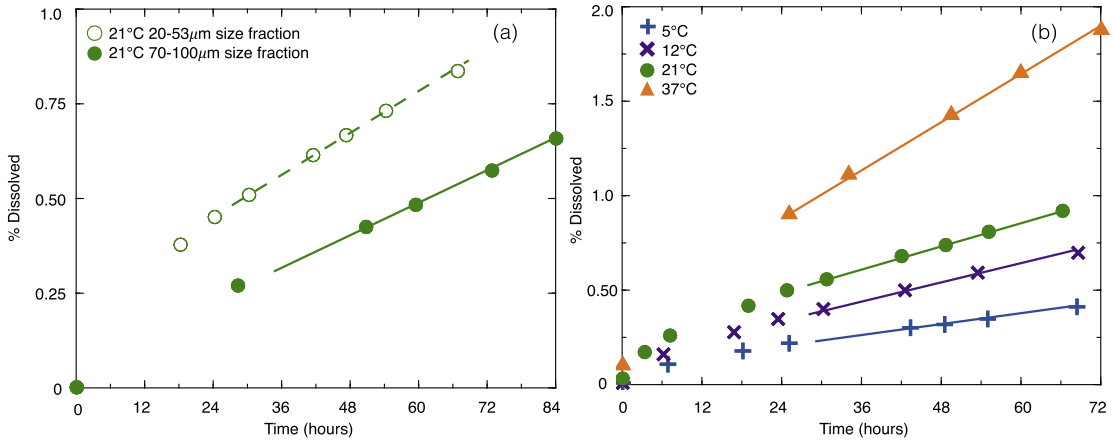

Fig. 1. (a) Raw dissolution vs. time of two different size fractions of ^{13}C-labeled calcite at $1-\Omega = 0.83$, normalized by the total fraction of powder dissolved. Curves become linear after 24 hours and the slope of the subsequent data points is taken as the rate (dashed/solid lines in the figure). The 20–53 μm size fraction dissolves more quickly than the 70–100 μm size fraction ($2.3{\cdot}10^{-3}$ vs. $1.4{\cdot}10^{-3}$ g/g/day), but both yield the same rate when corrected for BET surface area ($1.8{\cdot}10^{-13}$ mol/cm^2/s). (b) Raw dissolution vs. time at constant $1-\Omega = 0.80$. Increasing the temperature increases dissolution rate non-linearly.

Mehrbach et al.'s (1973) data, sulfate dissociation constants from Dickson et al. (1990), and a borate to salinity ratio from Uppström (1974).

Our dissolution rates were not affected by isotopic exchange. Experiments in supersaturated conditions ($\Omega = 1.3$) using the same methods saw no enrichment over the course of nine days beyond an initial increase in δ^{13}C of 1–3‰ (Subhas et al., 2015). Rate calculations rely on the rate of change of the δ^{13}C signal versus time, so the time independent exchange signal we observed does not alter our measurements of the net dissolution rate.

3. RESULTS

Fig. 2 shows our experimental results in the $1-\Omega$ framework. Data in this plot cover a range of DIC and alkalinity of 1740–2050 and 807–2045 μmol/kg, respectively, corresponding with a calculated pH range of 5.7–7.65 on the total proton scale (Fig. S2). Our methodology allowed for rate data from each individual experiment to be collected under conditions of constant solution saturation and unchanging mineral surface area. Typical δ^{13}C dissolution signals were on the order of 5-40‰, where a 20‰ increase corresponds to a decrease in surface height of ~7–8 nm, an addition of just 1 μmol/kg of alkalinity, and the release of 10^{-7} mole of calcium (Subhas et al., 2015). This is the first work to measure the near-equilibrium temperature dependence of calcite dissolution with this level of sensitivity, and our analytical constraints mean that the observed rate changes may be more directly attributed to temperature dependent effects on the dissolution mechanism.

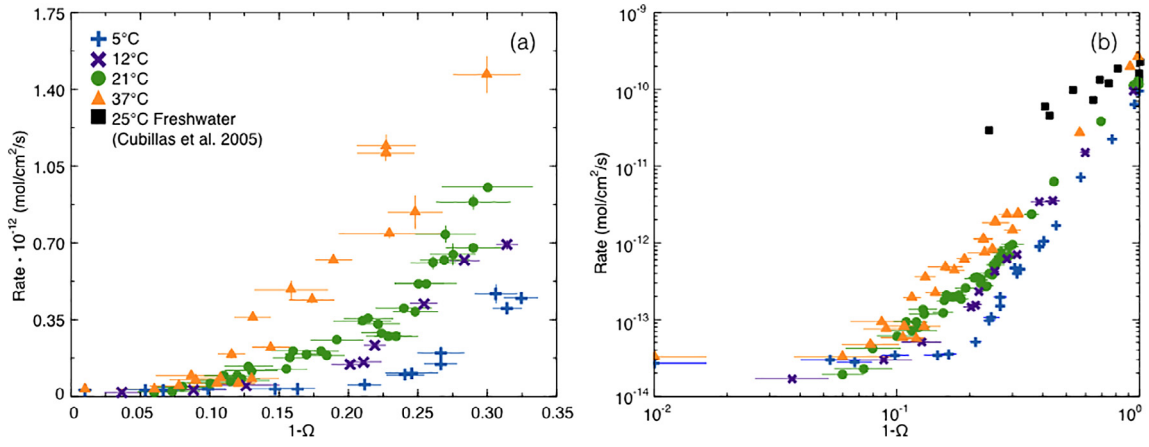

Fig. 2. Comparison of calcite dissolution rates (mol/cm^2/s) plotted vs. $1-\Omega$ (a) near equilibrium, and (b) in Log-Log $1-\Omega$ space from $1 > \Omega > 0$. Dissolution in seawater behaves differently than in freshwater (black squares in b). The y-error bars reflect the error on the linear fit to the dissolution vs. time data from 24 to 72 hours and do not include the uncertainty in surface area.

We can see from Fig. 2b that, although calcite dissolves at a similar rate in freshwater (Cubillas et al., 2005) and seawater at $\Omega \approx 0$, the mineral responds fundamentally differently in each media to changes in saturation state. The dissolution rate in freshwater increases almost linearly as Ω drops (left to right on the plot), but seawater dissolution is highly non-linear at all temperatures and consists of multiple different slopes in log-log space. Our data show that calcite dissolution rates increase by four orders of magnitude as Ω decreases from 1 to 0.

Calcite dissolution kinetics in seawater respond to temperature in a complex manner. Dissolution rates appear least sensitive to temperature for $\Omega > 0.9$, but they transition to a regime where the temperature sensitivity increases greatly from $0.9 > \Omega > 0.75$. This strong dependence weakens after $\Omega \approx 0.75$, and the rate offsets between each temperature remain nearly constant as the solution approaches $\Omega = 0$.

4. DISCUSSION

4.1. Analysis within the $1 - \Omega$ framework

Previous work in freshwater has successfully fit calcite dissolution kinetics with near-linear rate laws (Svensson and Dreybrodt, 1992; Cubillas et al., 2005), but it is clear that this approach cannot describe our seawater data. Our results are highly non-linear against $1 - \Omega$ and exhibit a similar trend far from equilibrium as observed in previous bulk dissolution experiments in seawater (Fig S3). Consistent with reports of a near equilibrium Ω_{crit} value in seawater (Subhas et al., 2015, 2017; Dong et al., 2018), we observe an abrupt change in the dissolution rate response to saturation at every temperature at $\Omega \approx 0.75$. Due to this change, no single rate law of the traditional $k(1 - \Omega)^n$ form can describe the dissolution rate of calcite across the full range of saturation states. York regression fits to the reaction orders (n) and net dissolution rate constants (k) are therefore calculated for data $\Omega < 0.75$ and $\Omega > 0.75$, with the results plotted in Fig. 3 and listed in Table 1.

The deeply undersaturated ($\Omega < 0.75$) rate constants agree with values typically reported for calcite in solutions above pH > 5 under atmospheric pCO_2 (order $1 \cdot 10^{-10}$ mol/cm^2/s, Plummer et al., 1978; Keir, 1980; Sjöberg and Rickard, 1985; Cubillas et al., 2005; Fischer and Lüttge, 2018; see also Table 5 in Subhas et al., 2015), and may be used to plot the expected behavior for a linear rate law by inserting them into Eq. (2c) with $n = 1$ (the dashed lines in Fig. 3). In the region near equilibrium that is most relevant to the modern ocean ($\Omega > 0.7$), linear kinetics overestimate our measured rates by more than two orders of magnitude. The use of smaller ks would reduce the difference between the calculated and actual rates near saturation, but the resulting fit would be entirely empirical and no longer grounded in the theory behind the $1 - \Omega$ rate law. Imposing linear kinetics also guarantees that dissolution rates across large ranges of Ω will be systematically over or underestimated. Our near equilibrium data require the reaction order to change with temperature from 0.34 to 2.47, and the rate constant to increase by over two orders of magnitude. These changes are interesting, but they represent simple curve fits and do not allow for meaningful mechanistic interpretations.

The temperature dependence of the far-from-equilibrium ks may still be used to gain insight into the dissolution mechanism. The apparent activation energy (E_a) of the dissolution reaction can be evaluated using the Arrhenius relation:

$$\ln(k) = \ln(A) - \frac{E_a}{R} \cdot \frac{1}{T} \quad (3)$$

Here, A is a pre-exponential factor (mol/cm^2/s), E_a is the apparent activation energy (kJ/mol), and R is the molar gas constant (kJ/mol/K). Plotting the far-from-equilibrium rate constants in Arrhenius space (Fig. 4) yields a value for E_a/R of -3021 ± 229, corresponding to an apparent activation energy of 25 ± 2 kJ/mol. This E_a agrees with results of previous studies in which calcite was dissolved in low pCO_2 media (Table 2), suggesting a common mechanism controls far-from-equilibrium dissolution regardless of the solution.

Calcite dissolution is linearly dependent on the concentration of H^+ for pH < 4–5, is transport limited, (Plummer et al., 1978, 1979; Busenberg and Plummer, 1986; Chou et al., 1989; Arakaki and Mucci, 1995; Alkattan et al., 1998), and exhibits a relatively small activation energy (8–10.5 kJ/mol Sjöberg and Rickard, 1984; Morse and Arvidson, 2002). Larger activation energies, like those compiled in Table 2 generally seen at higher pHs, indicate that dissolution is not purely transport limited and that additional reactions are occurring at the mineral surface (Sjöberg and Rickard, 1983; Morse and Arvidson, 2002). The exponential rate law (Eq. (2c)) is a statement of mechanism if the dissolution rate is linear ($n = 1$) versus undersaturation, but our data clearly show that n varies with Ω. Given the magnitude of the E_a and the strong non-linearity of our data, a different mechanistic framework is required to understand the near-equilibrium dissolution rate of calcite in seawater.

4.2. Identification of changes in dissolution mechanism

As did Subhas et al. (2017), we applied a mechanistic framework originally developed for crystal growth (Chernov, 1984; Malkin et al., 1989) that was subsequently and successfully adapted by Dove et al. (2005, 2008) to describe dissolution. Dove et al.'s work is based upon AFM observations of silica minerals dissolving at different solution undersaturations. The authors saw three distinct dissolution mechanisms: retreat of pre-existing steps at edges and screw dislocations near equilibrium, opening of 2D "pancake" etch pits at defects farther from equilibrium and, finally, opening of 2D etch pits homogenously across the mineral surface at deeper undersaturations (see schematic in Fig. 5). The onset of each mechanism was accompanied by an increase in dissolution rate. The same general transitions observed by Dove et al. (2005) for quartz dissolution also occur in the non-seawater dissolution of calcite (Teng, 2004), although the size and shape of calcite etch pits can differ from 2D "pancakes" due to interactions with ions

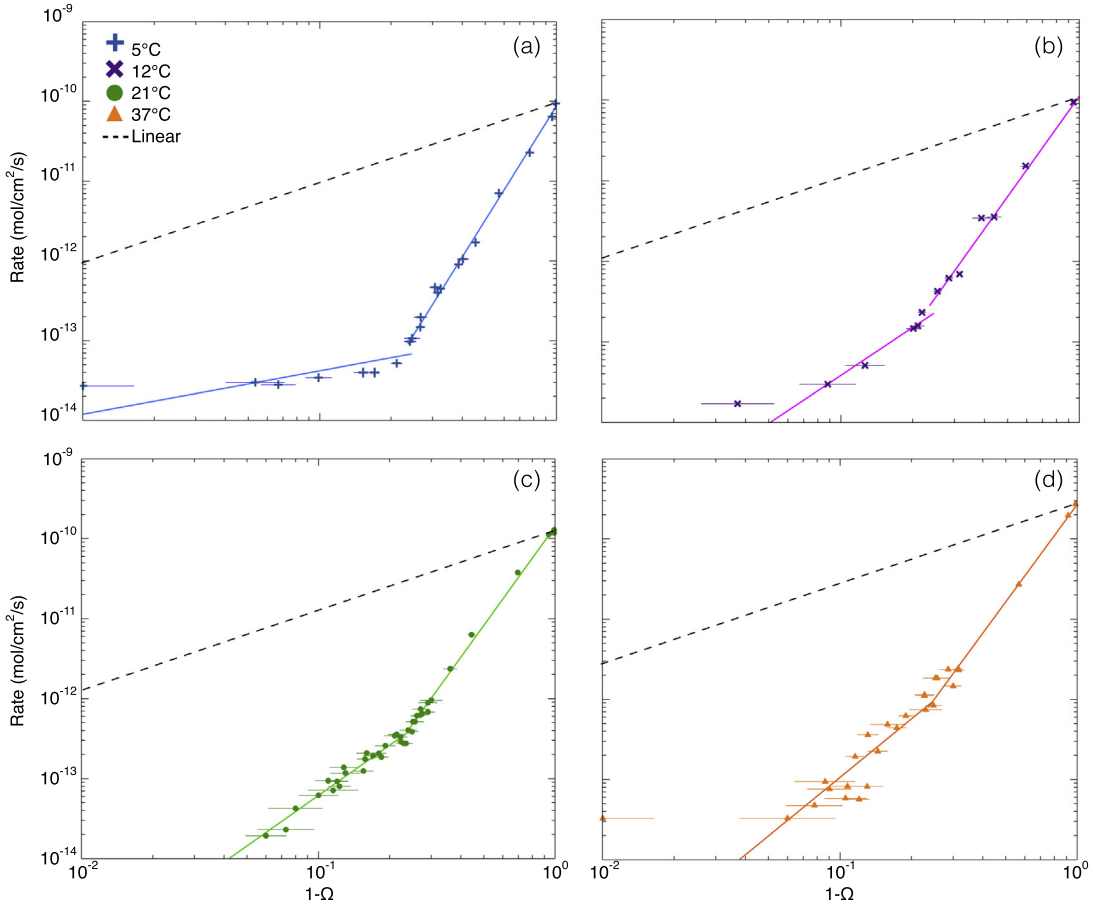

Fig. 3. Rate vs. $1-\Omega$ at 5 (a), 12 (b), 21 (c), and 37 °C (d) overlaid with best-fit lines to the data before and after $\Omega = 0.75$, not including data where $\Omega > 0.9$ (fitted values for k and n are listed in Table 1). The dashed lines in each panel show the expected behavior for a linear ($n = 1$) dissolution rate law. The linear rate law is anchored by the rate constant at $\Omega = 0$, and greatly overestimates dissolution near equilibrium.

Table 1
York fits to $\mathrm{Log(R)} = \mathrm{Log(k)} + \mathrm{nLog}(1-\Omega)$.

T (°C)	$\Omega > 0.75$		$\Omega < 0.75$	
	$\mathrm{Log_{10}k}$ (mol/cm²/s)	n	$\mathrm{Log_{10}k}$ (mol/cm²/s)	n
5	-13.07 ± 0.18	0.34 ± 0.09	-10.01 ± 0.10	4.81 ± 0.07
12	-11.51 ± 0.15	1.92 ± 0.07	-9.95 ± 0.27	4.09 ± 0.15
21	-11.06 ± 0.10	2.15 ± 0.05	-9.83 ± 0.12	4.18 ± 0.07
37	-10.50 ± 0.13	2.47 ± 0.05	-9.56 ± 0.35	4.58 ± 0.22

in solution (Ruiz-Agudo and Putnis, 2012; Klasa et al., 2013 and references therein). Other calcite dissolution models have been proposed (Lasaga and Lüttge, 2001; Fischer et al., 2012), but we continue with the Dove framework because it allows for the identification of dissolution mechanisms from bulk rate data and it can parse the effects of temperature on various kinetic and energetic parameters.

The exponential $1-\Omega$ framework only considers the solution saturation state, but the Dove framework allows for changes in dissolution mechanism and incorporates information about a crystal's physical and energetic properties. This information is encapsulated in two equations describing the three different dissolution mechanisms: one equation for the spread of 2D etch pits, and one for the retreat of pre-existing steps. Recent observations have demonstrated that etch pits spread via pulsing stepwaves in deeply undersaturated solutions, and that the speed of the wave varies with the distance from its source (Lasaga and Lüttge, 2001; Fischer and Lüttge, 2018). The Dove rate equations make the simplifying assumption that the step speed does not depend on the source, and therefore uses a single equation to describe both defect-assisted and homogenous dissolution. This assumption is likely valid for bulk dissolution, as step speeds converge on a constant

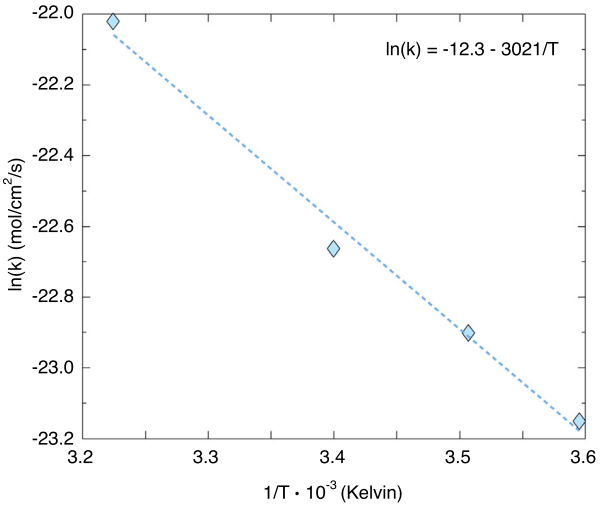

Fig. 4. Arrhenius plot of rate constants derived from far-from-equilibrium ($\Omega < 0.75$) experiments. A linear fit to the data yields a slope of -3021 ± 229 corresponding to an activation energy of 25 ± 2 kJ/mol.

Table 2
E_a Compilation for bulk calcite dissolution far from equilibrium.

Study	Solution	Temperature (°C)	pH	Ω	Activation energy (kJ/mol)
Plummer et al. (1978)	DI Water	5–60	2–5	0[a]	8.4 (from Eq. (5))
Salem et al. (1994)	DI Water	15–35	9.2	0–0.04	8.7
Sjöberg (1978)	0.7 M KCl	3–50	3.0	0[a]	10.5 (crystal)
Sjöberg and Rickard (1984)	0.7 M KCl	1–62	2.7–3.7	0[a]	13 ± 1 (Iceland Spar, from Fig. 7)
Finneran and Morse (2009)	0.07–5 M Ionic Media	25–85	5.5–6.5	0.4–0.8	20 ± 2
Gledhill and Morse (2006)	50–200 g/L Brine	25–82.5	5–6.2	0.2–1	21 ± 1
Gutjahr et al. (1996)	Ionic NaCl	20–70	7–9	0.4–1	24 ± 3 (k_{diss} from Table 2)
Sjöberg (1978)	0.7 M KCl	3–50	8.3	0[a]	25.7 (crystals) 35 (powder)
Sjöberg and Rickard (1984)	0.7 M KCl	1–62	8.4	0[a]	31–36 (Carrara Marble, Eq. 9)
Pokrovsky et al. (2009)	0.1 M NaCl, (pCO_2 2–50 atm)	25–100	4.0	0[a]	48.2 ± 4.6[b]
This study	Natural Seawater	5–37	5.5–6.5	0–0.75	25 ± 2

[a] Ω is not reported, but the solution composition suggests $\Omega = 0$.
[b] Pokrovsky et al. (2009) adjust this E_a to 14.7 ± 3.5 in the text when correcting for chemical transport.

value within a new nanometers from the pit source (Fischer and Lüttge, 2018). Full derivations of the Dove equations may be found in the appendix. The overall rate of dissolution by either defect-assisted or homogenous 2D etch pit growth (R_{2D}) is given by:

$$\ln\left(\frac{R_{2D}}{(1-\Omega)^{\frac{2}{3}}|\sigma|^{\frac{1}{6}}}\right) = \ln\left(h\beta C_e\left(\omega^2 h n_s a\right)^{\frac{1}{3}}\right) - \frac{\pi\alpha^2\omega h}{3(k_b T)^2}\left|\frac{1}{\sigma}\right| \quad (4a)$$

Here, the left hand term is now the normalized dissolution velocity (m/s), $|\sigma| = \ln(\Omega)$ is a measure of the solution driving force, h is the step height (m), β is the rate constant for surface retreat (step kinetic coefficient, m/s), ω is the molecular volume (m^3), n_s is the density of active nucleation sites (sites/m^2), a is the lattice spacing (m), α is the step edge free energy (mJ/m^2), k_b is Boltzmann's constant, T is the temperature (K), and C_e is the mineral solubility. The rate equations were derived for a single component crystal, so C_e has units of molecules/m^3. Calcite is a two component crystal, but we relate calcite K_{sp} (mol^2/kg^2) in seawater to C_e by assuming constant $[Ca^{2+}] = 0.01$ M, such that $K_{sp}/[Ca^{2+}] = C_e$ after converting from mol/kg to molecules/m^3.

Although it appears complex, Eq. (4a) describes a straight line with a slope set by a single term (the step edge free energy, α), and an intercept set collectively by the kinetic coefficient (β) and the number of active nucleation sites (n_s). All other terms are either fundamental mineral properties assumed to be constant (h, ω, a), or are determined by the experimental conditions (C_e, T, Ω, σ).

Dissolution by the retreat of pre-existing steps and screw dislocations (R_{step}) is given by a different equation:

$$\ln\left(\frac{R_{step}}{(1-\Omega)^{\frac{2}{3}}|\sigma|^{\frac{1}{6}}}\right) = \ln\left(\frac{\omega\beta C_e m h}{P}\right) + \ln\left((1-\Omega)^{\frac{1}{3}}\left|\frac{1}{\sigma}\right|^{\frac{1}{6}}\right) - \ln\left(1 + 8\left(\frac{\omega\alpha}{P k_b T}\right)\left|\frac{1}{\sigma}\right|\right) \quad (4b)$$

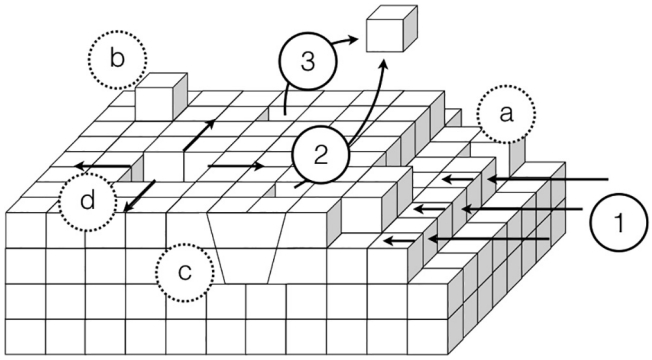

Fig. 5. Simplified model of a dissolving calcite crystal where each cube represents a $CaCO_3$ unit cell. Numbered arrows demonstrate different dissolution mechanisms, while letters show surface features. At low driving forces, dissolution is limited to the retreat of pre-existing steps (1), kinks (a), and adatoms (b). Steps are frequently sourced from screw dislocations, but are only shown at edges here for simplicity. Defects such as edge-dislocations (c) impart strain on the crystal lattice, resulting in localized areas of excess surface energy. As the solution becomes more undersaturated, these areas become available for defect-assisted 2D dissolution (2). At even greater undersaturations, 2D dissolution occurs homogenously across the calcite surface (3) without the need for pre-existing defects. Both (2) and (3) produce 2D etch pits (d) that will propagate radially until they reach the edge of the mineral or encounter another etch pit and are eliminated.

Here, the added terms are the number of elementary steps (m, order 1) and the perimeter of the screw dislocation core sourcing the steps (P, proportional to $2\pi mh$).

An advantage of this model is that bulk rate data exhibit distinct slopes when plotted as normalized rate versus $\left|\frac{1}{\sigma}\right|$ (Fig. 6), depending on the dominant dissolution mechanism. Even though both homogenous and defect-assisted dissolution are fit by Eq. (4a), we can distinguish between them based upon the distance from equilibrium. By definition, homogenous dissolution has a greater number of nucleation sites than defect-assisted dissolution. Data collected during homogenous dissolution are therefore expected to have a greater y-intercept than for defect-assisted dissolution. Additionally, we would expect the defect-assisted mechanism to have a shallower slope versus $\left|\frac{1}{\sigma}\right|$, as defects impose strain on the calcite surface and locally decrease the free energy of step formation per unit step height (α). The step-retreat mechanism is described by Eq. (4b), and curves upwards versus $\left|\frac{1}{\sigma}\right|$. Under this set of equations, it is important to note that the *absolute* rate always decreases as the solution approaches equilibrium (Fig. 3), and it is only the *normalized* rate that increases. The apparent increase near equilibrium is driven by the third term in Eq. (4b), where we take the natural log of $(1-\left|\frac{1}{\sigma}\right|)$ (α is negative), and $\left|\frac{1}{\sigma}\right|$ becomes very large, and ultimately undefined, as Ω approaches 1.

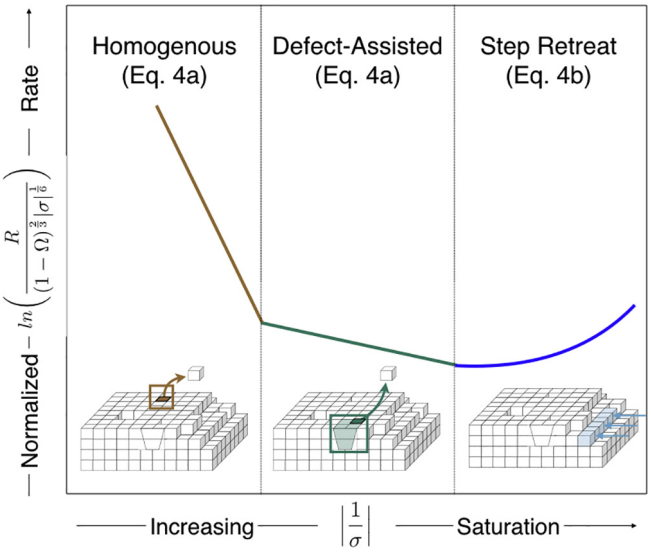

Fig. 6. Expected data trends as the calcite surface transitions between dissolution mechanisms. Far from equilibrium (left panel), 2D etch pits open homogenously across the surface and the data are described by Eq. (4a). At intermediate driving forces, 2D dissolution may only proceed at defects (middle panel). Very near equilibrium, the solution driving force is only strong enough to support dissolution at pre-existing steps or screw dislocations (right panel). Data resulting from step retreat are described by Eq. (4b). Absolute rates of dissolution are slowest for step retreat, but the normalized rate curves upwards versus $\left|\frac{1}{\sigma}\right|$ as the solution approaches equilibrium.

Our results are plotted across the full range of saturations in Fig. 7, and they demonstrate each of the three expected trends in the surface framework. The non-linear nature of the x-axis emphasizes data collected at $\Omega > 0.95$, so the axis is truncated from $0<\left|\frac{1}{\sigma}\right| < 25$ ($0 < \Omega < 0.96$) in Fig. 8a–d to help view the data and fits more clearly. All temperatures exhibit a steep linear slope where $\left|\frac{1}{\sigma}\right| < 3.5$ ($\Omega < 0.75$). Closer to equilibrium, dissolution at 12, 21, and 37 °C shifts to a shallower linear slope, but this is not observed in the 5 °C data. Experimental dissolution rates measured at 12 and 37 °C begin to 'curve upwards' after $\left|\frac{1}{\sigma}\right| > 10$ ($\Omega > 0.9$, see also Fig. 7).

We interpret each of the slope changes as mechanistic transitions that occur as the solution approaches equilibrium and falls below two critical energy barriers. Seawater calcite dissolution is dominated by homogenous etch pit formation from $\Omega = 0$ to $\Omega \approx 0.75$, at which point etch pit formation may only occur at defects. These defect-assisted etch pits set the dissolution rate between $\Omega \approx 0.75$ and $\Omega \approx 0.9$, and dissolution at higher saturation states may only occur at pre-existing steps on edges and at screw dislocations. At 5 °C, dissolution appears to skip over the defect-assisted mechanism and instead transitions directly to the step-retreat mechanism.

The critical Ωs for mechanistic transitions that we have identified in seawater are much closer to equilibrium than they are in freshwater. Compared to observations by Teng (2004) in weak electrolyte solutions, the Ω_{crit} for the opening of defect-assisted etch pits in seawater is $\Omega = 0.9$ versus $\Omega = 0.54$, and the Ω_{crit} for homogenous etch pit formation (defined by Teng as Ω_{max}) is $\Omega = 0.75$ versus $\Omega = 0.007$. The rate of seawater calcite dissolution will be set by the density of pre-existing steps for $\Omega > 0.9$, and by the defect-density for $\Omega_{crit} > \Omega > \Omega_{max}$ ($0.9 > \Omega > 0.75$). At colder temperatures relevant to the deep ocean, dissolution will be set by the density of pre-existing steps for $1 > \Omega > 0.75$. Once homogenous 2D dissolution is activated at $\Omega < \Omega_{max}$ ($\Omega < 0.75$), the overall rate will be limited by the maximum pit spreading rate.

The shift of calcite-seawater mechanistic transitions towards equilibrium is significant because it means that any model based upon a single rate equation, regardless of its reaction order, will not accurately capture dissolution responses to changes in saturation state. Our results suggest that typical ocean water column Ωs (>0.7) and temperatures (≤5 °C) currently limit calcite to dissolution at pre-existing steps, but the oceans are acidifying due to fossil fuel burning and lowering both calcite and aragonite saturation states (Feely et al., 2004; Doney et al., 2009; Byrne et al., 2010; Feely et al., 2012). These perturbations in Ω may activate new surface mechanisms and elicit highly non-linear dissolution responses, both due to absolute changes in Ω and as regions where $\Omega < 1$ occur in warmer waters. As a rough comparison, we can calculate the magnitude of the offset between oceanographic models that assume linear ($n = 1$) kinetics for Eq. (2c) (Hales and Emerson, 1997; Dunne et al., 2012; Ilyina and Zeebe, 2012) and our 5 °C data. Arbitrarily beginning with a total alkalinity of 2230 μmol/kg at surface pressure, calcite is saturated ($\Omega = 1$) at a pH of ~ 7.6 at 5 °C. Decreasing the pH by 0.1 units lowers Ω from 1.0 to ~0.8, maintaining step retreat as the rate-determining mechanism at 5 °C and minimally affecting calcite dissolution rates. Further decreasing pH by 0.1 units drops Ω from ~0.8 to ~0.65, activating homogenous dissolution of the calcite surface. This second pH drop would increase calcite dissolution rates by a factor of ~25, whereas linear kinetics would predict only a factor

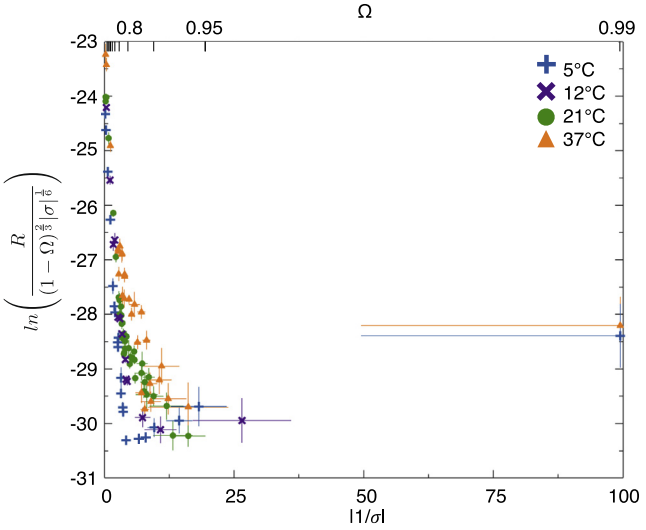

Fig. 7. The same data as in Fig. 2b, but recast as dissolution velocity (m/s) vs. $\left|\frac{1}{\sigma}\right|$ over the full range of undersaturations ($0 < \Omega < 0.99$). Saturation state increases from left to right. Rates at 5, 12, and 37 °C "curve upwards" as Ω approaches equilibrium, indicating dissolution by retreat of pre-existing steps. Tick marks on the top axis show Ω in increments of 0.1, with an additional tick at 0.95 to emphasize the highly non-linear nature of $\left|\frac{1}{\sigma}\right|$ axis.

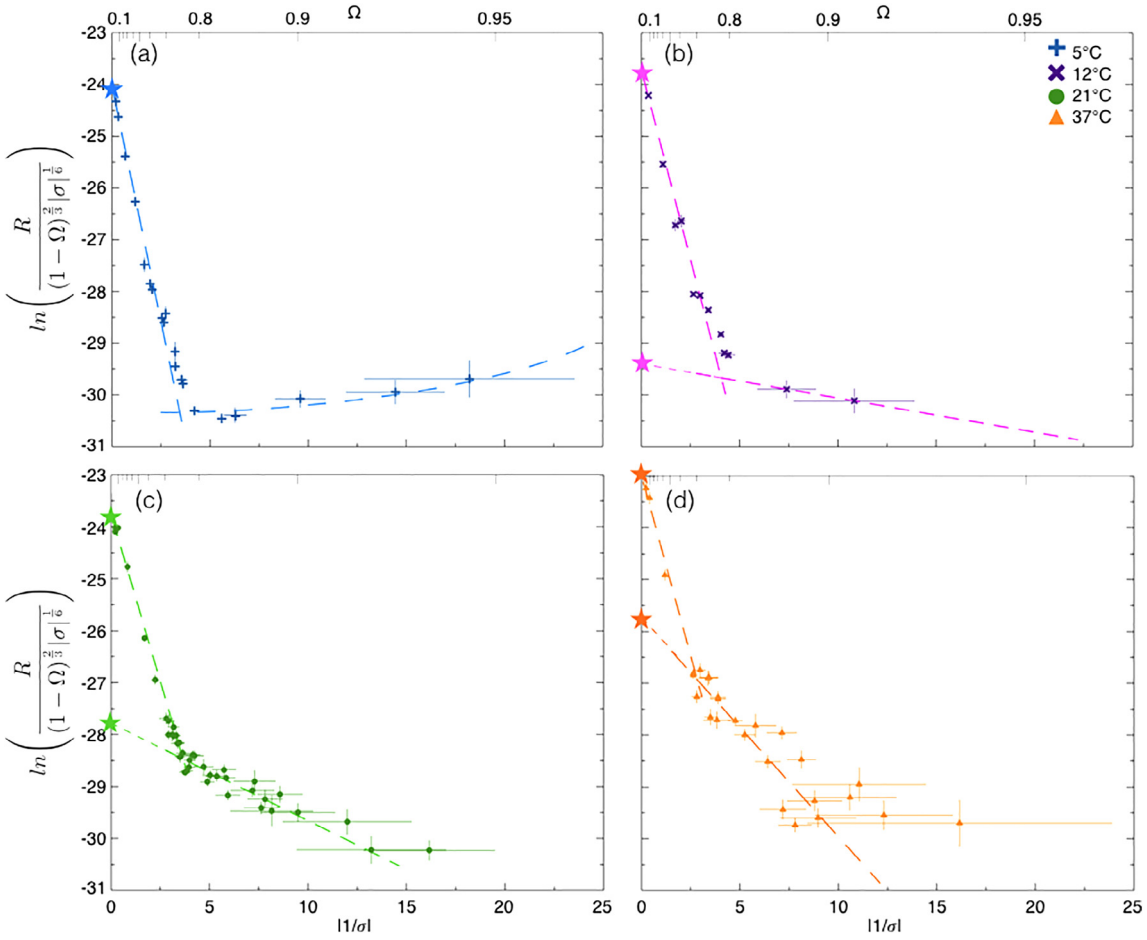

Fig. 8. Dissolution velocities (m/s) at 5 (a), 12 (b), 21 (c), and 37 °C (d) from $0<\left|\frac{1}{\sigma}\right|<25$ ($0<\Omega<0.96$). Saturation increases from left to right. All temperatures are fit to Eq. (4a) from $0<\left|\frac{1}{\sigma}\right|<3.5$. 12, 21, 37 °C are fit to Eq. (4a) between $3.5<\left|\frac{1}{\sigma}\right|<25$ while 5 °C is fit to Eq. (4b). The intercepts (stars on Y-axis) and slopes of the fits to Eq. (4a) are presented in Table 3.

of ~2. The discrepancy between the different rate laws will only widen as the oceans continue to acidify.

Models based upon the non-linear $n = 4.5$ reaction order from Keir (1980) (Archer, 1991; Berelson et al., 1994; Jahnke et al., 1994; Archer, 1996; Jansen et al., 2002; Archer et al., 2009) are similarly inadequate to describe dissolution. The high reaction order employed in these models is only applicable for $0 < \Omega < 0.75$ (Table 2) and does not capture the change in dissolution response when transitioning mechanisms near equilibrium. We find that the dissolution rate at 5 °C is relatively constant versus Ω for $1 > \Omega > 0.75$, so a reaction order of $n = 4.5$ will correctly predict far-from-equilibrium dissolution while systematically underestimating rates near equilibrium. A more appropriate approach would be to employ two different rate equations at 5 °C, one for step retreat $\Omega > 0.75$, and one for homogenous dissolution $\Omega < 0.75$. This recommendation maintains the simplicity of the empirical rate equation while accounting for changes in dissolution mechanism.

4.3. Using temperature dependence to extract physical and energetic parameters of calcite dissolution in seawater

The inherent variability in step and defect densities between minerals complicate rate comparisons between studies (Arvidson et al., 2003; Fischer et al., 2014), but we can still advance our knowledge of calcite dissolution kinetics by analyzing the temperature dependence of our results within the surface framework. All of our calcite powders were sourced from the same batch and may be presumed to have the same initial step and defect densities. Tight control of solution saturation means that dissolution rate changes within each mechanistic regime may be directly related to the temperature dependence of fundamental physical and energetic properties in the calcite-seawater system. We step through each mechanism and calculate step edge free energies (α), kinetic coefficients (β), and active nucleation site densities (n_s). We also use the temperature dependencies of β and n_s to estimate the activation energy for detachment from retreating steps (ϵ_{step}) and the kinetic

energy barrier for removing an ion to initiate an etch pit (ϵ_{init}).

The fitted slopes and intercepts (Fig. 8) are resolved for both homogenous and defect-assisted etch pit formation (Table 3); the cutoff of each fit is set to $\left|\frac{1}{\sigma}\right| = 3.5$ ($\Omega = 0.75$) to remain consistent with our analysis in the $1-\Omega$ framework. Our results are not sensitive to the precise cutoff choice. As noted in Section 4.2, dissolution at 5 °C appears to skip over the defect-assisted mechanism, so only $\left|\frac{1}{\sigma}\right| < 3.5$ for the 5 °C data is included in our analysis of etch pit dissolution. The 5 °C data have the highest density of measurements near equilibrium, so it will be used later to evaluate the energetics of the step retreat mechanism.

By analyzing the fits to Eq. (4a) and making some simplifying assumptions, we can extract the physical parameters β, n_s, and α, and clarify their roles in setting the overall dissolution rate as a function of temperature. The intercepts and slopes are plotted in Fig. 9 for homogenous ($0 < \left|\frac{1}{\sigma}\right| < 3.5$) and defect-assisted ($3.5 < \left|\frac{1}{\sigma}\right| < 10$) dissolution. The data are linear versus $1/T^2$ and are fit according to:

$$\text{Intercept}_{2D} = \ln\left(h\beta C_e\left(\omega^2 h n_s a\right)^{\frac{1}{3}}\right) = I_o + I_1 \cdot \frac{1}{T^2} \tag{5a}$$

$$\text{Slope}_{2D} = -\frac{\pi\alpha^2\omega h}{3(k_b T)^2} = S_o + S_1 \cdot \frac{1}{T^2} \tag{5b}$$

such that the overall rate is given by:

$$\begin{aligned}\text{Rate}_{2D} &= \text{Intercept}_{2D} + \text{Slope}_{2D} \cdot \left|\frac{1}{\sigma}\right| \\ &= \left(I_o + I_1 \cdot \frac{1}{T^2}\right) + \left(S_o + S_1 \cdot \frac{1}{T^2}\right) \cdot \left|\frac{1}{\sigma}\right|\end{aligned} \tag{5c}$$

Table 3
Fits to Eq. (4a) for 2D Dissolution.

T (°C)	Homogenous dissolution $0.01 < \lvert 1/\sigma \rvert < 3.5$		Defect-assisted dissolution $3.5 < \lvert 1/\sigma \rvert < 25$	
	Intercept $\ln(h\beta C_e(\omega^2 h n_s a)^{\frac{1}{3}})$	Slope $\frac{\pi\alpha^2\omega h}{3(k_b T)^2}$	Intercept $\ln(h\beta C_e(\omega^2 h n_s a)^{\frac{1}{3}})$	Slope $\frac{\pi\alpha^2\omega h}{3(k_b T)^2}$
5	-24.02 ± 0.02	-1.83 ± 0.04	N/A	N/A
12	-23.71 ± 0.04	-1.47 ± 0.03	-29.40 ± 0.90	-0.07 ± 0.11
21	-23.75 ± 0.01	-1.29 ± 0.03	-27.79 ± 0.25	-0.19 ± 0.04
37	-23.00 ± 0.11	-1.39 ± 0.06	-25.74 ± 0.26	-0.42 ± 0.05

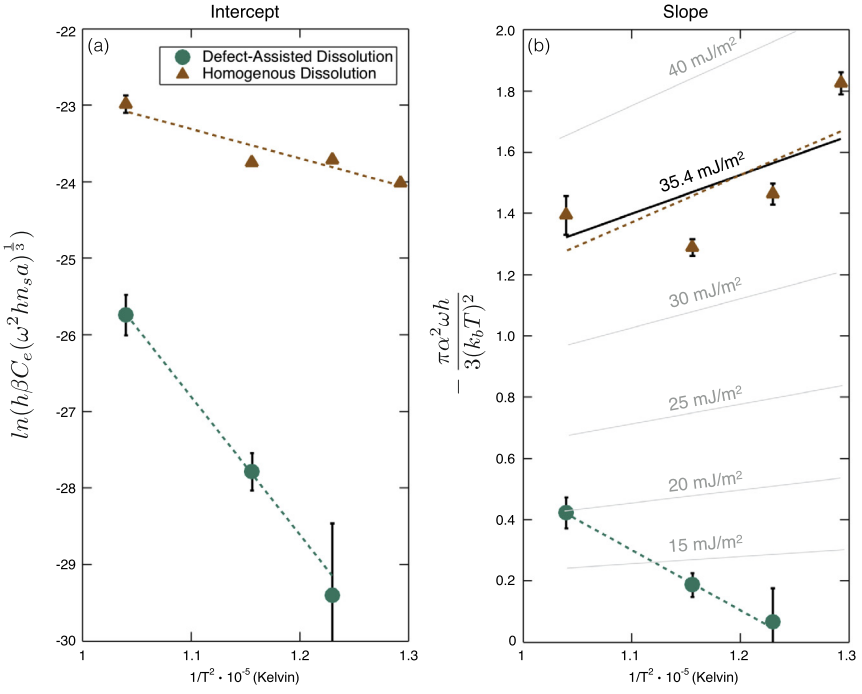

Fig. 9. Temperature dependence of kinetic and energetic parameters of calcite dissolution in seawater. (a) Change in the intercept (proportional to β and n_s) and (b) slope (proportional to α) of the fit to Eq. (4a) for homogenous ($0 < \left|\frac{1}{\sigma}\right| < 3.5$, triangles) and defect-assisted ($3.5 < \left|\frac{1}{\sigma}\right| < 25$, circles) dissolution. Lines for constant α are plotted in (b) for comparison with the data. Fits to the data are presented in Table 4.

I_1 and S_1 describe the temperature sensitivities of the intercept (proportional to β and n_s) and slope (proportional to α) terms of Eq. (4a). The values of I_o, I_1, S_o, and S_1 are listed in Table 4.

4.3.1. Dissolution by Homogenous Etch Pit Formation

Homogenous dissolution exhibits a relatively weak temperature dependence in its β and n_s terms (Fig. 9a). We can isolate the effect of β on the intercept term by making the simplifying assumptions that β is independent of Ω and that n_s is saturated at its maximum value when calcite is undergoing homogenous 2D dissolution. Direct observations of homogenous 2D calcite dissolution in non-seawater solutions place the maximum n_s between 10^{12} (Teng, 2004) and 10^{13} sites/m^2 (Ruiz-Agudo et al., 2009). Assuming an average n_s of $5 \cdot 10^{12}$ sites/m^2, we solve for β using the fitted intercepts (Table 3), rearranging Eq. (5a), and substituting in the constants given in Table 5. The resulting βs are 0.40 $\pm$ 0.02, 0.54 $\pm$ 0.05, 0.53 $\pm$ 0.01, and 1.17 $\pm$ 0.26 cm/s at 5, 12, 21, and 37 °C, respectively.

The βs we derive agree with those observed in AFM studies in non-seawater solutions. In the surface nucleation equations, the speed of a moving step, v, is related to β and the solution saturation state via (Chernov, 1984; Malkin et al., 1989):

$$v = \omega\beta C_e(1 - \Omega) \quad (6)$$

By extrapolating to $\Omega = 0$ and substituting the values for w, C_e, and β at each temperature, we calculate upper limits for v of 6.2, 7.8, 10.3, and 16.4 nm/s at 5, 12, 21, and 37 °C, respectively. Although faster than typical calcite values of 0.5–4 nm/s (Lea et al., 2001; De Giudici, 2002; Arvidson et al., 2006; Harstad and Stipp, 2007; Ruiz-Agudo et al., 2009), they are in the range for observations at the edges of coalescing etch pits of 7.9–14.3 nm/s (Vinson and Luttge, 2005). Etch pit coalescence is expected when the calcite surface is saturated with nucleation sites, so our high step speeds support our assumption that the mechanism in this Ω region is homogenous 2D etch pit formation. We note that these equivalences of β are based upon non-seawater measurements of n_s. If the saturated value of n_s is different in seawater, then our βs will change accordingly.

We can use the temperature dependence of our derived kinetic coefficients to estimate the activation energy of

Table 4
Coefficients for the Observed Temperature Effect on the Intercepts and Slopes of Eq. (4a) for 2D Dissolution.

	I_0	$I_1 \cdot 10^5$	S_0	$S_1 \cdot 10^5$
Homogenous $0.01 < \lvert 1/\sigma \rvert < 3.5$	-19.1 ± 1.18	-3.8 ± 1.0	0.33 ± 1.2	-1.5 ± 1.0
Defect-Assisted $3.5 < \lvert 1/\sigma \rvert < 25$	-5.82 ± 1.29	-19.1 ± 1.1	-2.38 ± 0.12	1.9 ± 0.1

Table 5
Constants and calculated values for β, n_s and α.

Variable	Units	Temperature (°C) 5	12	21	37	Source
m	–	1	1	1	1	–
h	m	$3 \cdot 10^{-10}$	$3 \cdot 10^{-10}$	$3 \cdot 10^{-10}$	$3 \cdot 10^{-10}$	1
a	m	$3 \cdot 10^{-10}$	$3 \cdot 10^{-10}$	$3 \cdot 10^{-10}$	$3 \cdot 10^{-10}$	1
w	m^3	$6.12 \cdot 10^{-29}$	$6.12 \cdot 10^{-29}$	$6.12 \cdot 10^{-29}$	$6.12 \cdot 10^{-29}$	2
P	m	$1.88 \cdot 10^{-9}$	$1.88 \cdot 10^{-9}$	$1.88 \cdot 10^{-9}$	$1.88 \cdot 10^{-9}$	3
K_{sp}	mol^2/kg^2	$4.309 \cdot 10^{-7}$	$4.318 \cdot 10^{-7}$	$4.296 \cdot 10^{-7}$	$4.151 \cdot 10^{-7}$	4
C_e	atoms/m^3	$2.595 \cdot 10^{22}$	$2.600 \cdot 10^{22}$	$2.587 \cdot 10^{22}$	$2.500 \cdot 10^{22}$	5
		Homogenous 2D Dissolution (Eq. (4a))				
$n_{s\_homogenous}$	sites/m^2	$5 \cdot 10^{12}$	$5 \cdot 10^{12}$	$5 \cdot 10^{12}$	$5 \cdot 10^{12}$	1, 6
β_{2D}	m/s	$4.0 \pm 0.02 \cdot 10^{-3}$	$5.4 \pm 0.05 \cdot 10^{-3}$	$5.3 \pm 0.01 \cdot 10^{-3}$	$11.7 \pm 0.26 \cdot 10^{-3}$	This study
$\alpha_{homogenous}$	mJ/m^2	-37.6 ± 0.7	-34.5 ± 0.8	-33.2 ± 0.7	-36.5 ± 1.6	This study
		Defect-Assisted 2D Dissolution (Eq. (4a))				
n_{s_defect}	sites/m^2	–	$4.7 \pm 1.2 \cdot 10^5$	$2.5 \pm 0.1 \cdot 10^7$	$1.3 \pm 0.9 \cdot 10^9$	This study
α_{defect}	mJ/m^2	–	-6.8 ± 5.9	-12.7 ± 2.7	-20.1 ± 2.3	this study
		Step-Propagation (Eq. (4b))				
β_{step}	m/s	$3 \cdot 10^{-7}$	–	–	–	This study
α_{step}	mJ/m^2	-0.5	–	–	–	This study

[1] Teng (2004).
[2] From calcite density of 2.71 g/cm^3.
[3] Estimated assuming a burgers vector $b = mh$. $P = 2\pi b$, analogously to Dove et al. (2005).
[4] CO2SYS equilibrium K_{sp} in seawater at each temperature. Sal = 35 psu.
[5] $K_{sp}/[Ca^{2+}]$, converted to molecules/m^3. $[Ca^{2+}] = 0.01$ M.
[6] Ruiz-Agudo et al. (2009).

detachment from steps (ϵ_{step}) on the calcite surface. β is related to ϵ_{step} via an Arrhenius-style relation (Chernov, 1984; Malkin et al., 1989; Zhang and Nancollas, 1992; Xu et al., 2010, Eq. (A.8) in appendix), and measuring the slope of ln(β) versus 1/T yields a value of -2700 ± 700, corresponding with an ϵ_{step} of -22 ± 6 kJ/mol (Fig. 10a). This is the first estimate of ϵ_{step} for calcite dissolution in seawater. It agrees with the value of -25 ± 6 kJ/mol derived from AFM measurements of β for obtuse step retreat (Xu et al., 2010), further lending confidence to the strength and sensitivity of our bulk solution measurement approach.

Our calculated ϵ_{step} in seawater is not significantly different from that in freshwater, suggesting that changes in absolute ionic strength (IS) have little effect on step detachment energetics. Few studies have specifically measured the effect of IS on ϵ_{step}, so we cannot make a direct comparison with past research. The results are also unclear for the effects of IS on the bulk calcite dissolution/precipitation rate. Several studies have shown little to no effect of IS on calcite dissolution (Rickard and Sjöberg, 1983; Buhmann, 1987; Pokrovsky et al., 2005) and precipitation (Zhong and Mucci, 1989) rate, while others have found IS to catalyze precipitation (Zuddas and Mucci, 1998) and inhibit dissolution (Gledhill and Morse, 2006; Finneran and Morse, 2009). More remains to be done to understand how calcite dissolution mechanisms are affected by IS.

Our results further suggest that the sharp increase in rate at $\Omega \approx 0.75$, that has been reported in previous seawater studies (Berner and Morse, 1974; Keir, 1980; Subhas et al., 2015, 2017; Dong et al., 2018), occurs when calcite transitions from defect-assisted to homogenous 2D dissolution after overcoming a critical step edge free energy. β and n_s provide kinetic information on the dissolving calcite surface (i.e., how fast etch pits spread and how many sites are actively dissolving), but they do not tell us anything about the energetic constraints for when homogenous dissolution is activated. For this, we can look at the slopes of the data below $\left|\frac{1}{\sigma}\right| < 3.5$, as they are proportional to α. The calculated slopes (Table 3) are plotted in Fig. 9b versus $1/T^2$ and overlaid with lines of constant α. The overlaid lines trend downward with increasing temperature because the slope term in Eq. (4a) also contains $1/T^2$. The trend for homogenous dissolution (Fig. 9b triangles) follows a line of constant $\alpha = -35.4$ mJ/m^2. Though the scatter appears large, the squared dependence on α means that the step edge free energies are well constrained. Averaging the α values in Table 5 across temperatures yields -35.4 ± 2.0 mJ/m^2. This α is lower, but of the same order of magnitude as the 60–68 mJ/m^2 range calculated for the spontaneous precipitation of calcite in non-seawater solutions (Koutsoukos and Kontoyannis, 1984; Pokrovsky, 1998a). Our observation suggests that homogenous dissolution is activated on the calcite surface once a critical surface energy barrier, $\alpha_{homogenous} = -35.4 \pm 2.0$ mJ/m^2, is surpassed, regardless of temperature. It may also explain our earlier observation in Section 4.1 for why bulk dissolution studies historically recover similar rates far from equilibrium in seawater. Each study had surpassed $\alpha_{homogenous}$ and was measuring the dissolution rate of a single mechanism, homogenous 2D etch pit formation.

4.3.2. Dissolution by defect-assisted etch pit formation

Temperature has a much larger effect in the region $3.5 < \left|\frac{1}{\sigma}\right| < 10$ associated with defect-assisted dissolution. According to Fig. 9a, the fitted intercepts for defect-assisted dissolution decrease with temperature by nearly four natural log units, compared to just one for homogenous dissolution. To understand this dependence, we must again attempt to distinguish between the effects of β and n_s on the intercept term of Eq. (4a). We can no longer assume a constant n_s, but our analysis of homogenous dissolution provides new constraints on the values and temperature dependencies of β. Both mechanisms initiate differently, but once started, they

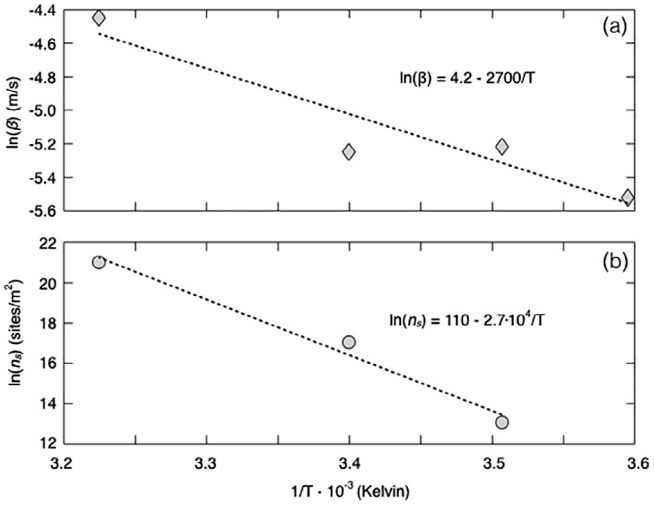

Fig. 10. Arrhenius plots for the kinetic coefficient (a) and nucleation site density (b) derived from fits to Eq. (4a). (a) The slope of ln(β) versus 1/T is -2700 ± 700, corresponding to an activation energy of detachment from kinks/steps of 22 ± 6 kJ/mol. (b) The slope of ln(n_s) versus 1/T is $2.7 \pm 0.4 \cdot 10^4$, corresponding to a kinetic energy barrier to etch pit initiation of -230 ± 30 kJ/mol.

are assumed to proceed via the same opening and spreading of 2D pits. We therefore assume that the same βs that we calculated for homogenous dissolution also apply for defect-assisted dissolution. We refer to this shared term as β_{2D} and list its values in Table 5. Given this assumption, we solve for n_s by again rearranging the intercept term and substituting in the constants and β_{2D} from Table 5. We calculate active nucleation site densities of $4.7 \pm 1.2 \cdot 10^5$, $1.3 \pm 0.1 \cdot 10^7$, and $1.8 \pm 0.9 \cdot 10^9$ sites/m^2 at 12, 21, and 37 °C, respectively. Increasing temperature increases the number of pit nucleation sites.

The temperature dependence of n_s is related to the kinetic energy barrier for removing an ion from the surface to initiate an etch pit, ϵ_{init}. (Eq. (A.9) in appendix, Dove et al., 2005). This energy barrier is distinct from the step edge free energy, as ϵ_{init} is related to initiating an etch pit, whereas α is related to stabilizing an etch pit. Newly initiated pits will quickly be eliminated unless a critical free energy barrier, that is in turn dependent on α, T, and Ω per Eq. (A.6), is surpassed. Taking the natural log of n_s versus 1/T gives a value of $-2.7 \pm 0.4 \cdot 10^4$, corresponding with an ϵ_{init} of -230 ± 30 kJ/mol (Fig. 10b). This is the first time that ϵ_{init} has been estimated for calcite in seawater.

It is evident that the slope term for defect-assisted dissolution is strongly temperature dependent in a way that is not explained by the theory and runs counter to what was observed for homogenous dissolution. Whereas homogenous dissolution follows the prediction for a single, critical $\alpha_{homogenous}$, the energy barrier for defect-assisted dissolution, α_{defect}, changes by nearly a factor of three (S_1 terms in Table 4) and has the opposite temperature dependence. This suggests that opposing kinetic and energetic effects set the overall rate of defect-assisted dissolution. Temperature has a positive effect on calcite dissolution rate by increasing n_s and β, allowing for more active nucleation sites and faster pit spreading rates. Warmer temperatures also increase the local step edge free energy, though, making it more difficult to form a stable etch pit. The change in the temperature trend of α implies that there are additional factors beyond α, β, and n_s that influence near-equilibrium dissolution rates.

4.3.3. Dissolution by retreat of pre-existing steps

It is difficult to set experimental waters to Ωs very near equilibrium, but the limited number of points we have suggest that dissolution initiates via step retreat at all temperatures and continues from just under saturation until an Ω_{crit} near 0.9. Dissolution at 5 °C skips the defect-assisted mechanism seen at warmer temperatures and maintains the curved slope indicative of step retreat (Eq. (4b)) from saturation until $\Omega \approx 0.75$ (Fig. 7). Substituting in the constants in Table 5 to Eq. (4b), the 5 °C data from $3.5 < \left|\frac{1}{\sigma}\right| < 25$ fit a step edge free energy of -0.5 mJ/m^2 and a β_{step} of $3 \cdot 10^{-5}$ cm/s. The kinetic coefficient required to fit the data is four orders of magnitude smaller than that used for homogenous/defect-assisted dissolution, but similar discrepancies between mechanisms have been seen in other minerals (Dove et al., 2005).

Of the temperatures investigated in this study, the 5 °C experiments are most relevant to the modern ocean. The 5 °C results are also the first evidence that the onset of a dissolution mechanism may be temperature dependent in seawater. We are unable to say with certainty why the defect-assisted dissolution mechanism is not activated, but one hypothesis is that the kinetic energy barrier to etch pit initiation is too large for etch pits to form at defects at 5 °C. Projecting back the fitted intercept for defect-assisted dissolution reported in Table 4, we calculate an active nucleation site density of only 5 sites/cm^2 at 5 °C. Considering that our grain size is on the 10 s to 100 s of microns scale, this would essentially mean that there are zero etch pits forming at defects. In this case, only step retreat is possible until the solution driving force overcomes $\alpha_{homogenous}$ and initiates homogenous dissolution.

Calcite has been shown to undergo simultaneous dissolution and precipitation across the full range of Ωs (Arakaki and Mucci, 1995; Subhas et al., 2017), so it is also possible that a temperature dependent change in the balance of these gross fluxes could explain the behavior we observe at 5 °C. Precipitation is known to be influenced by the temperature and Mg:Ca ratio of the solution (Mucci and Morse, 1983, 1984; Mucci, 1986), and temperature dependent step changes in behavior have already been observed in the calcite system (Morse et al., 1997). Precipitation occurs preferentially at high-energy sites (Burton and Cabrera, 1949; Burton et al., 1951), so any change in its rate could suppress the formation of etch pits at defects. This effect would be amplified if there were few available defects. Since back-precipitation may be identified on our calcite grains by areas of elevated ^{12}C (Subhas et al., 2017), we will be able to quantify the role of back-precipitation in the future by dissolving calcite surfaces near equilibrium at low temperatures.

4.4. Role of solution chemistry

The surface theory has provided valuable insights into calcite dissolution mechanisms across a wide range of saturation states, but phenomena such as the reversal of the temperature dependence of α and the skipping of defect-assisted dissolution at 5 °C indicate that the theory is not complete. The surface framework we have used contains only indirect information about the chemical speciation of the solution and the mineral surface itself, despite the known importance of these effects (Arakaki and Mucci, 1995; Pokrovsky et al., 2009; Sand et al., 2016 and references therein). The surface model encapsulates all the effects of speciation in its step edge free energy term. This is because α is dependent upon the local crystal bonding environment, and this bonding environment is affected by interactions with ions in solution (Chernov, 1984). The speciation of the calcite surface is well understood in dilute solutions (Van Cappellen et al., 1993; Pokrovsky, 1998b; Pokrovsky and Schott, 2002; Pokrovsky et al., 2005; Wolthers et al., 2008; Schott et al., 2009), and significant work has been done to relate these species to dissolution and precipitation kinetics (Chou et al., 1989; Arakaki and Mucci, 1995; Pokrovsky and Schott, 2002; Pokrovsky et al., 2005, 2009; Wolthers et al., 2012). Surface speciation models have only recently begun to include interactions

with individual major seawater ions such as SO_4^{2-} and Mg^{2+} (Song et al., 2017; Dobberschütz et al., 2018, and references therein), and these models have yet to be applied to the kinetics of seawater dissolution. Our measurements imply that a complete understanding of a dissolution rate law for calcite in seawater will require a surface energetic framework that incorporates the chemical complexation of the solution and mineral surface.

The role of solution chemistry on the dissolution rate of calcite in seawater has been supported by recent work by Subhas et al. (2017) using carbonic anhydrase (CA) to increase the re-equilibration rate of H_2CO_3 in seawater. With the addition of CA, the authors observed a ~250× increase in calcite dissolution rates above $\Omega > 0.7$, compared to seawater at the same pH without CA. This saturation region is associated with defect-assisted dissolution, which is the mechanism we found to have the strongest temperature dependence. Given that the rate constant for the hydration of $CO_{2(aq)}$ to H_2CO_3 increases exponentially with temperature in dilute solutions (Wang et al., 2010), it is possible that the behavior we have observed for $\Omega > 0.75$ may be partially explained by an elevation in the formation rate of H_2CO_3. Future work evaluating the temperature dependence of calcite dissolution in the presence of carbonic anhydrase will help to further parse the effects of solution chemistry and surface processes on the overall dissolution rate.

5. CONCLUSIONS

We dissolved ^{13}C-labeled calcite in seawater over a range of temperatures and found that the dissolution rate is highly non-linear across the full range of saturations. Although we recovered the same activation energy and dissolution rates at $\Omega = 0$ as those found in non-seawater solutions, the strong non-linearity of our data near equilibrium necessitated the use of a different mechanistic model beyond the traditional, empirical rate law, $R = k(1 - \Omega)^n$. Using a surface-based framework developed by Dove et al. (2005), we found that our results were consistent with calcite dissolution being dominated by the retreat of pre-existing steps for $1 > \Omega > 0.9$, defect-assisted etch pit formation for $0.9 > \Omega > 0.75$, and homogenous etch pit formation for $\Omega < 0.75$. Calcite surface energetics are dramatically altered by seawater, as the mechanistic transitions we identified occur significantly closer to equilibrium than they do in dilute solutions. The shift towards equilibrium suggests that ocean acidification may cause marine carbonates to enter faster dissolution regimes more readily than anticipated from previous studies. Our work also provides the first seawater estimates of kinetic coefficients (β), nucleation site densities (n_s), and step edge free energies for each mechanism (α), as well as the activation energy for detachment from steps (ϵ_{step}) and the kinetic energy barrier to etch pit initiation (ϵ_{init}). Several unexplained phenomena suggest that a complete theory will require the combination of a chemical speciation model with knowledge of the rate constants and energies we have measured for each of calcite's dissolution mechanisms.

ACKNOWLEDGEMENTS

We would like to thank the anonymous journal reviewers as well as Oleg Pokrovsky and Henry Teng for the insightful comments and suggestions they gave that helped to improve this manuscript. This material is based upon work supported by the National Science Foundation Graduate Research Fellowship under Grant No. 1745301, as well as NSF grant Numbers OCE1220302, OCE1559004 and 1559215. John Naviaux and Adam Subhas would also like to thank the Resnick Sustainability Institute at Caltech for fellowship support.

A. APPENDIX

Dove et al. (2005) found that the same equations originally developed to describe crystal growth (Burton et al., 1951; Chernov, 1984; Malkin et al., 1989) could also be used to describe dissolution. Although developed for a single component crystal, we step through the model below as it may still provide useful insight into the behavior of $CaCO_3$. According to the surface model, dissolution occurs via the consecutive removal of crystal layers, where each dissolving layer has a defined thickness, h (step height, nm), and retreats along the face of the crystal with a velocity, v (cm/s). There can be several, simultaneous dissolution fronts, and the average spacing between them, λ (nm), influences the overall rate. Closer spacings (smaller λ) allow for more dissolution fronts and a faster rate, whereas farther spacings (larger λ) can only support slower rates. Conceptualized this way, the normalized dissolution rate (length/-time) is given by

$$R = \frac{hv}{\lambda} \tag{A.1}$$

The generalized form of Eq. (A.1) holds true for dissolution mechanisms that are not limited by the rate of transport to/from the mineral surface (see Table A1).

The retreat velocity, v, is linearly dependent on the step kinetic coefficient for the solid, the thermodynamic driving force, and the volume element being dissolved. It is classically formulated as (Chernov, 1984; Malkin et al., 1989)

$$v = \omega\beta C_e(1 - \Omega) \tag{A.2}$$

where β is the step kinetic coefficient (cm/s), ω is the molecular volume (cm^3) and C_e is the equilibrium concentration of dissolved species in solution (molecules/cm^3).

The step spacing is the only term in Eq. (A.1) that changes depending on the dissolution mechanism, and it is therefore what sets the functional form of the rate equation. At low driving forces near $\Omega \approx 1$, dissolution occurs primarily via the retreat of pre-existing steps at edges and/or screw dislocations. The step spacing is then derived assuming spiral retreat around a dislocation exceeding a "critical radius," r_c, that is set by the local bonding environment of the crystal and the solution driving force. It is given by (Chernov, 1984; Chernov et al., 1986)

$$\lambda = \frac{8r_c + P}{m} \text{ with } r_c = -\frac{\omega\alpha}{k_b T|\sigma|};\ |\sigma| = \ln(\Omega) \tag{A.3}$$

Table A1
Carbonate system parameters and dissolution rates for all experiments presented in this study. DIC and Alk are listed with ± 1σ standard errors. Ω and pH are calculated by inputting DIC and Alk pairs into CO2SYS with errors propagated via Monte-Carlo analysis. ΔG is calculated from saturation state, where $\Delta G = RT\ln(\Omega)$.

T (°C)	Size (μm)	Expt.	DIC (μmol/kg)	Alk (μmol/kg)	Ω	pH	ΔG (kJ/mol)	Rate			
								$\cdot 10^{-3}$ (g/g/day)	BET $\cdot 10^{-13}$ (mol/cm^2/s)	Geo $\cdot 10^{-13}$ (mol/cm^2/s)	% Err
5	70–100	T6B1	2012 ± 2	1998 ± 1	0.76 ± 0.01	7.52	−0.64	0.76	0.97	3.27	4.6
		T6B2	2013 ± 3	1998 ± 0	0.75 ± 0.02	7.51	−0.65	0.84	1.07	3.58	3.3
		T6B3	2012 ± 1	1971 ± 3	0.60 ± 0.02	7.41	−1.20	8.26	10.52	35.3	3.1
		T11B1	2008 ± 4	1991 ± 2	0.73 ± 0.03	7.52	−0.72	1.54	1.97	6.60	14.2
		T11B2	2017 ± 4	1993 ± 1	0.70 ± 0.02	7.49	−0.84	2.39	3.05	10.2	9.0
		T11B3	2015 ± 4	1997 ± 1	0.73 ± 0.02	7.52	−0.72	1.16	1.48	4.96	3.4
		T11B4	2010 ± 4	2021 ± 2	0.95 ± 0.02	7.63	−0.13	0.24	0.30	1.00	12.1
		T11B5	2018 ± 4	2036 ± 2	0.99 ± 0.02	7.65	−0.02	0.21	0.27	0.91	16.7
		T12B1	2013 ± 1	2022 ± 2	0.93 ± 0.01	7.62	−0.16	0.22	0.28	0.94	9.4
		T12B2	2010 ± 1	1985 ± 2	0.69 ± 0.01	7.49	−0.87	3.15	4.02	13.5	5.5
		T12B3	2011 ± 2	2001 ± 2	0.79 ± 0.01	7.55	−0.55	0.41	0.52	1.73	3.7
		T12B4	2012 ± 2	1985 ± 0	0.68 ± 0.01	7.48	−0.91	3.53	4.50	15.1	4.6
		T12B5	2013 ± 1	2018 ± 2	0.90 ± 0.01	7.60	−0.24	0.27	0.34	1.14	6.5
	20–53	T26B4	2010 ± 1	1986 ± 2	0.69 ± 0.02	7.49	−0.85	6.19	4.67	11.4	9.5
		T41B4	2052 ± 3	2040 ± 2	0.79 ± 0.03	7.54	−0.54	0.62	0.46	1.13	0.0
		T27B1	2019 ± 1	1937 ± 1	0.43 ± 0.01	7.29	−1.96	93.3	70.3	171	7.2
		T27B2	2012 ± 1	1839 ± 4	0.23 ± 0.01	7.04	−3.40	301	227	552	2.6
		T43B3	2033 ± 1	1993 ± 3	0.61 ± 0.02	7.43	−1.13	12.0	9.03	21.97	1.9
		T50B5	2048 ± 2	2044 ± 2	0.85 ± 0.02	7.57	−0.37	0.46	0.35	0.84	11.7
		T50B6	2049 ± 2	2043 ± 0	0.84 ± 0.01	7.56	−0.41	0.47	0.35	0.86	10.6
		T24B1	1892 ± 2	810 ± 7	0.01 ± 0.00	5.93	−11.2	1248	9401	2288	2.4
		T24B2	1971 ± 1	1396 ± 5	0.04 ± 0.00	6.44	−7.21	846	638	1551	3.0
12	20–53	T40B3	2042 ± 2	2041 ± 2	0.91 ± 0.02	7.48	−0.22	0.40	0.30	0.73	1.6
		T40B4	2045 ± 2	2027 ± 0	0.79 ± 0.01	7.42	−0.56	2.09	1.57	3.82	1.3
		T40B5	2042 ± 1	2012 ± 1	0.72 ± 0.01	7.38	−0.79	8.21	6.19	15.1	1.8
		T40B6	2046 ± 1	2011 ± 1	0.69 ± 0.01	7.36	−0.89	9.16	6.91	16.8	3.1
		T40B1	1921 ± 10	1427 ± 14	0.06 ± 0.00	6.43	−6.70	1244	938	2281	3.1
		T40B2	2039 ± 10	1936 ± 4	0.41 ± 0.03	7.14	−2.14	201	151	368	3.6
		T42B1	2034 ± 2	2017 ± 0	0.80 ± 0.01	7.43	−0.53	1.93	1.46	3.54	1.7
		T42B2	2031 ± 2	2025 ± 2	0.87 ± 0.02	7.46	−0.32	0.67	0.51	1.23	1.8
		T42B3	2039 ± 1	2019 ± 1	0.78 ± 0.01	7.42	−0.59	3.09	2.33	5.67	2.4
		T42B4	2033 ± 1	2009 ± 1	0.75 ± 0.01	7.40	−0.70	5.61	4.23	10.3	1.2
		T42B5	2027 ± 3	1979 ± 6	0.61 ± 0.03	7.31	−1.17	45.5	34.3	83.4	5.0
		T42B6	2035 ± 1	1976 ± 7	0.56 ± 0.03	7.28	−1.37	46.7	35.2	85.7	5.3
		T44B3	2031 ± 1	2036 ± 1	0.96 ± 0.01	7.51	−0.09	0.23	0.17	0.42	11.4

21	70–100	B42-B1	2026 ± 1	2019 ± 1	0.94 ± 0.01	7.35	−0.15	0.15	0.19	0.65	2.9
		T1B1	2029 ± 3	2017 ± 1	0.92 ± 0.02	7.33	−0.21	0.33	0.42	1.42	2.6
		T8B1	2007 ± 3	1995 ± 1	0.90 ± 0.02	7.33	−0.26	0.48	0.61	2.05	2.3
		T8B2	2001 ± 2	1989 ± 1	0.89 ± 0.01	7.33	−0.29	0.74	0.94	3.16	5.9
		T8B3	2007 ± 1	1967 ± 4	0.71 ± 0.03	7.23	−0.83	6.96	8.86	29.7	4.1
		T8B4	2004 ± 2	1964 ± 3	0.71 ± 0.02	7.23	−0.85	5.32	6.77	22.7	3.2
		T9B2	1999 ± 2	1985 ± 1	0.88 ± 0.01	7.32	−0.31	0.73	0.93	3.10	8.8
		T9B3	2001 ± 1	1965 ± 3	0.73 ± 0.02	7.25	−0.76	5.81	7.39	24.8	5.2
		T9B4	1990 ± 3	1963 ± 1	0.79 ± 0.02	7.28	−0.59	2.69	3.43	11.5	1.8
		T4B2	2003 ± 4	1962 ± 5	0.70 ± 0.03	7.23	−0.86	7.50	9.55	32.0	2.0
		T14B1	2008 ± 1	1994 ± 1	0.87 ± 0.02	7.33	−0.35	0.92	1.17	3.91	0.8
		T14B2	2013 ± 1	1994 ± 1	0.84 ± 0.02	7.32	−0.42	1.63	2.08	6.96	2.1
		T14B4	2016 ± 1	1996 ± 1	0.83 ± 0.02	7.32	−0.44	1.44	1.83	6.14	3.0
		T16B1	2025 ± 3	1995 ± 2	0.78 ± 0.01	7.27	−0.62	2.28	2.90	9.73	3.0
		T16B4	2029 ± 1	1999 ± 2	0.79 ± 0.02	7.27	−0.59	2.79	3.55	11.9	0.8
		T16B6	2022 ± 2	1997± 2	0.81 ± 0.02	7.29	−0.52	2.39	3.04	10.2	5.3
		T18B5	2023 ± 3	1990 ± 2	0.76 ± 0.02	7.26	−0.67	3.17	4.04	13.5	2.2
		T18B6	2024 ± 2	1990 ± 2	0.75 ± 0.02	7.26	−0.70	3.03	3.86	12.9	5.4
		T20B1	1891 ± 4	807 ± 10	0.01 ± 0.00	5.75	−11.23	925	1178	3950	0.6
		T20B2	1866 ± 4	808 ± 11	0.01 ± 0.00	5.76	−11.16	1001	1274	4274	0.4
	20–53	T25B4	2010 ± 2	1956 ± 4	0.64 ± 0.02	7.19	−1.09	31.1	23.5	57.1	3.8
		T30B3	2022 ± 1	1998 ± 2	0.82 ± 0.01	7.29	−0.50	2.46	1.86	4.52	2.4
		T30B4	2022 ± 1	1998 ± 2	0.82 ± 0.01	7.29	−0.49	2.74	2.07	5.03	3.0
		T28B2	1991 ± 2	1965 ± 2	0.78 ± 0.02	7.28	−0.61	4.38	3.30	8.03	2.5
		T31B4	2022 ± 6	1987 ± 2	0.75 ± 0.02	7.25	−0.71	6.81	5.13	12.5	1.9
		T33B3	2029 ± 2	2008 ± 2	0.84 ± 0.02	7.29	−0.41	1.64	1.24	3.00	1.7
		T33B4	2027 ± 1	2006 ± 2	0.84 ± 0.01	7.30	−0.42	2.33	1.76	4.27	1.6
		T34B1	2031 ± 2	1999 ± 2	0.77 ± 0.02	7.26	−0.64	3.64	2.75	6.68	3.2
		T36B6	2029 ± 2	2014 ± 3	0.88 ± 0.03	7.32	−0.30	0.95	0.71	1.73	9.3
		T39B1	2045 ± 2	2006 ± 2	0.74 ± 0.02	7.24	−0.74	8.07	6.09	14.8	4.9
		T39B2	2042 ± 2	2002 ± 2	0.73 ± 0.02	7.24	−0.77	8.24	6.21	15.1	2.2
		T39B3	2036 ± 3	1999 ± 2	0.74 ± 0.02	7.25	−0.72	6.80	5.13	12.5	2.3
		T50B7	2020 ± 2	1998 ± 2	0.83 ± 0.02	7.30	−0.46	2.57	1.94	4.71	5.7
		T34B1	2031 ± 2	1999 ± 2	0.77 ± 0.02	7.26	−0.64	3.64	2.75	6.68	3.2
		T34B2	2032 ± 2	1999 ± 2	0.77 ± 0.02	7.26	−0.65	3.64	2.74	6.67	1.5
		T25B4	2010 ± 2	1956 ± 4	0.64 ± 0.02	7.19	−1.09	31.1	23.5	57.1	3.8
		T26B2	2007 ± 2	1936 ± 4	0.56 ± 0.02	7.13	−1.43	83.5	63.0	153	2.8
		T26B3	2000 ± 2	1839 ± 7	0.30 ± 0.01	6.89	−2.91	502	379	921	9.2
		T24B4	1948 ± 2	1402 ± 8	0.06 ± 0.00	6.29	−6.90	1496	1128	2743	1.6
	[a]	T28B1	1993 ± 1	1962 ± 2	0.76 ± 0.01	7.27	−0.66	3.29	2.48	6.03	5.4
	[a]	T30B3	2022 ± 1	1998 ± 2	0.82 ± 0.01	7.29	−0.50	2.46	1.86	4.52	2.4
	[a]	T34B8	2030 ± 5	1998 ± 2	0.77 ± .03	7.26	−0.65	5.56	4.19	10.2	4.5
	[b]	T31B5	2026 ± 6	1986 ± 2	0.72 ± 0.02	7.24	−0.79	8.59	6.48	15.8	7.9
	[b]	T33B1	2027 ± 2	2011 ± 2	0.87 ± 0.02	7.30	−0.34	1.83	1.38	3.35	9.8
	[b]	T33B2	2026 ± 1	2010 ± 2	0.88 ± 0.01	7.30	−0.32	1.06	0.80	1.94	3.1
	[c]	T44B1	2038 ± 2	2028 ± 2	0.93 ± 0.02	7.34	−0.19	0.30	0.23	0.56	4.1

(*continued on next page*)

Table A1 (*continued*)

T (°C)	Size (μm)	Expt.	DIC (μmol/kg)	Alk (μmol/kg)	Ω	pH	ΔG (kJ/mol)	Rate			
								$\cdot 10^{-3}$ (g/g/day)	BET $\cdot 10^{-13}$ (mol/cm^2/s)	Geo $\cdot 10^{-13}$ (mol/cm^2/s)	% Err
37	70–100	T15B3	2008 ± 5	1959 ± 2	0.83 ± 0.02	7.04	−0.49	3.45	4.40	14.8	3.8
		T15B4	2010 ± 4	1958 ± 2	0.81 ± 0.01	7.03	−0.54	4.89	6.22	20.9	2.2
		T17B3	2001 ± 4	1966 ± 0	0.91 ± 0.03	7.09	−0.23	0.86	1.10	3.67	7.2
		T17B4	1999 ± 3	1966 ± 1	0.92 ± 0.02	7.09	−0.21	0.37	0.47	1.59	5.6
		T17B5	2000 ± 3	1965 ± 1	0.91 ± 0.02	7.09	−0.24	0.59	0.76	2.54	8.0
		T19B1	2024 ± 2	2004 ± 1	1.02 ± 0.02	7.13	0.06	0.00	N/A	N/A	N/A
		T19B2	2018 ± 3	1981 ± 0	0.89 ± 0.02	7.07	−0.29	0.64	0.82	2.75	7.8
		T19B3	2022 ± 3	1980 ± 0	0.87 ± 0.02	7.06	−0.36	0.64	0.82	2.74	6.1
		T19B4	2023 ± 2	2005 ± 0	0.99 ± 0.01	7.13	−0.03	0.26	0.33	1.10	10.7
		T22B1	2019 ± 7	1953 ± 3	0.74 ± 0.03	7.00	−0.76	14.4	18.4	61.6	3.7
		T22B2	2018 ± 6	1953 ± 3	0.75 ± 0.03	7.00	−0.75	14.4	18.3	61.3	2.8
		T28B4	1989 ± 2	1950 ± 2	0.88 ± 0.01	7.07	−0.33	0.44	0.56	1.89	5.1
		T30B1	1997 ± 5	1926 ± 2	0.70 ± 0.02	6.98	−0.92	11.5	14.6	49.1	5.8
		T30B2	2005 ± 1	1963 ± 2	0.87 ± 0.01	7.07	−0.36	2.84	3.62	12.1	4.0
		T30B5	2014 ± 1	1969 ± 2	0.86 ± 0.01	7.06	−0.40	1.76	2.24	7.51	4.9
		T31B1	2005 ± 1	1917 ± 1	0.63 ± 0.01	6.93	−1.18	16.8	21.4	71.8	1.1
	20–53	T27B4	1984 ± 7	1838 ± 2	0.43 ± 0.02	6.78	−2.16	360	271	659	8.5
		T25B1	1737 ± 2	807 ± 9	0.02 ± 0.00	5.70	−10.63	3601	2715	6602	20.1
		T25B2	1904 ± 15	1394 ± 4	0.09 ± 0.00	6.19	−6.33	2616	1972	4796	11.8
		T35B2	2027 ± 7	1965 ± 2	0.77 ± 0.04	7.01	−0.67	9.84	7.42	18.0	3.0
		T36B5	2003 ± 3	1957 ± 3	0.84 ± 0.03	7.05	−0.45	6.44	4.86	11.8	8.9
		T37B1	2040 ± 4	1978 ± 2	0.77 ± 0.02	7.01	−0.66	15.2	11.4	27.8	4.5
		T37B2	2040 ± 4	1978 ± 2	0.77 ± 0.02	7.01	−0.66	14.7	11.1	27.0	3.3
		T37B3	2040 ± 4	1966 ± 4	0.71 ± 0.02	6.98	−0.87	31.2	23.5	57.2	6.0
		T37B4	2030 ± 4	1964 ± 2	0.75 ± 0.02	7.00	−0.74	11.1	8.40	20.4	9.2
		T38B1	2040 ± 2	1960 ± 1	0.69 ± 0.01	6.96	−0.98	32.0	24.1	58.6	5.2
		T38B2	2041 ± 3	1961 ± 2	0.68 ± 0.02	6.96	−0.98	31.0	23.3	56.6	2.3
		T38B3	2044 ± 3	2003 ± 2	0.89 ± 0.02	7.07	−0.29	0.77	0.58	1.41	1.5
		T38B4	2037 ± 4	2003 ± 2	0.94 ± 0.03	7.09	−0.16	0.43	0.33	0.79	6.2
		T28B3	1989 ± 1	1951 ± 2	0.88 ± 0.01	7.08	−0.32	2.57	1.94	4.72	10.1

[a] Sieved in pH 8.5 ammonium hydroxide.
[b] Baked at 80C under vacuum for one week after sieving in ammonium hydroxide.
[c] Sieved in $\Omega = 1$ Dickson seawater.

where m is the number of elementary steps (order 1), P is the perimeter of the core of the dislocation (proportional to $2\pi mh$), k_b is Boltzmann's constant, T is the temperature (Kelvin), $|\sigma| = \ln(\Omega)$ is a measure of the solution driving force, and α is the free energy of step formation per unit step height (mJ/m^2). A larger α implies a slower dissolution rate, as the formation/retreat of a step produces a greater increase in the local surface energy of the crystal. The step edge free energy varies depending upon the local bonding environment of the material, where the bonding environment is affected by solid-solid interactions (whether dissolution is at a kink, step, dislocation, flat surface, etc.) and solid-solution interactions (changes in the chemical speciation of the surface). α is therefore distinct from the average surface energy of a perfect crystal (Burton and Cabrera, 1949; Burton et al., 1951; Cabrera et al., 1954; Cabrera and Levine, 1956; Chernov, 1984).

As the solution undersaturation increases, 2D etch pits begin to form first at crystal defects, and then homogenously across the mineral surface. Although step-retreat continues, it is limited to a single direction (the direction of the step), so its contribution to the overall rate is small once the production and radial spread of etch pits is activated. 2D dissolution therefore changes the dominant shape of the dissolving front from a spiral (Eq. (A.3)) to a spreading area, and in doing so changes the relevant step spacing to use in Eq. (A.1).

The spacing of etch pits of average area, λ^2, is related to the speed of propagation (v from Eq. (A.2)) and the steady-state rate of pit opening, J ($cm^{-2}\,s^{-1}$). The lifetime of a pit is given by (Chernov, 1984).

$$\frac{\lambda}{v} = \frac{1}{J}\frac{1}{\lambda^2} \tag{A.4}$$

Substituting (A.4) into (A.1) gives a new equation that describes the rate of 2D dissolution, either at defects or homogenously across the surface.

$$R_{2D} = h\left(v^2 J\right)^{\frac{1}{3}} \tag{A.5}$$

Eq. (A.5) may be further expanded to account for the solution's effect on the steady-state rate of pit opening, J. The rate of pit opening depends on two things: the frequency of new site formation (sites/time) and the probability of surpassing some critical free energy barrier, ΔG^{2D}_{Crit}. The overall energy barrier is, in turn, a function of the *local* step edge free energy α, and the driving force of the solution, σ. It is given by (Malkin et al., 1989)

$$\Delta G^{2D}_{Crit} = -\frac{\pi\alpha^2\omega h}{k_b T|\sigma|} \tag{A.6}$$

We can see from Eq. (A.6) that the required ΔG^{2D}_{Crit} to stabilize and open a pit decreases for constant α as the solution becomes more undersaturated (greater $|\sigma|$). The frequency of new site formation is related to the density of active nucleation sites (n_s, sites/cm^2), the lattice spacing (a, nm), and the spreading rate constant for the material (β).

The probability of opening a pit is set by ΔG^{2D}_{Crit} via an Arrhenius-style relation, where the pre-exponential factor contains the steady-state frequency of new site formation, $n_s a\beta$.

$$J = J_0 \exp\left(-\frac{\Delta G^{2D}_{Crit}}{k_b T}\right) \text{ with } J_0 = |\sigma|^{\frac{1}{2}} n_s a h C_e \beta \tag{A.7}$$

The step height, h, and the lattice spacing, a, are physical properties of the mineral that do not change with temperature or solution undersaturation. C_e exhibits a temperature dependence, but this effect is well documented in seawater (Mehrbach et al., 1973; Dickson and Millero, 1987) and simple to account for in the model. Therefore, the crystal parameters in J_0 that set the overall, steady-state nucleation rate are the density of active pit nucleation sites, n_s, and the step kinetic coefficient, β.

β is expected to exhibit temperature dependence according to (Chernov, 1984; Malkin et al., 1989; Zhang and Nancollas, 1992; Xu et al., 2010):

$$\beta = \beta_0 \exp\left(-\frac{\epsilon_{step}}{k_b T}\right) \tag{A.8}$$

Here, the interpretation of ϵ_{step} changes depending upon which of two potential dissolution pathways is occurring. In the first pathway, the dissolving species directly detaches from a kink/step and enters the solution. In the second pathway, the species does not directly detach, but instead diffuses away from a kink/step to become an adatom that can subsequently desorb from the surface. ϵ_{step} in the first case is the energy of direct detachment from a kink/step, and ϵ_{step} in the second case is the energy of surface diffusion. Surface diffusion is hindered on calcite by water (Liang and Baer, 1997) and dipoles on the calcite surface (Gratz et al., 1993), so ϵ_{step} in our system is the energy of direct detachment from kinks/steps.

n_s exhibits a temperature dependence according to (Chernov, 1984; Chernov et al., 1986; Dove et al., 2005):

$$n_s = n_{s0} \exp\left(-\frac{\epsilon_{init}}{k_b T}\right) \tag{A.9}$$

Here, ϵ_{init} is the kinetic energy barrier for removing a species from the surface to initiate a new etch pit. ϵ_{init} is distinct from Eq. (A.6) because, while etch pits can initiate on the surface, they will not be stable and propagate across the mineral face unless ΔG^{2D}_{Crit} has also been surpassed. The pre-exponential factors in Eqs. (A.8) and (A.9) contain entropy terms (Burton et al., 1951).

Substituting Eqs. (A.7), (A.6) and (A.2) into (A.5) and rearranging yields an equation describing dissolution by either homogenous or defect-assisted 2D dissolution (Eq. (4a) in the text)

$$\ln\left(\frac{R_{2D}}{(1-\Omega)^{\frac{2}{3}}|\sigma|^{\frac{1}{6}}}\right) = \ln\left(h\beta C_e\left(\omega^2 h n_s a\right)^{\frac{1}{3}}\right) - \frac{\pi\alpha^2\omega h}{3\left(k_b T\right)^2}\left|\frac{1}{\sigma}\right| \tag{A.10}$$

We arrive at a similar equation for dissolution by step retreat by substituting Eq.'s (A.3) and (A.2) into (A.1) and rearranging (Eq. (4b) in the text)

$$\ln\left(\frac{R_{step}}{(1-\Omega)^{\frac{2}{3}}|\sigma|^{\frac{1}{6}}}\right) = \ln\left(\frac{\omega\beta C_e m h}{P}\right) + \ln\left((1-\Omega)^{\frac{1}{3}}\left|\frac{1}{\sigma}\right|^{\frac{1}{6}}\right) - \ln\left(1+8\left(\frac{\omega\alpha}{Pk_bT}\right)\left|\frac{1}{\sigma}\right|\right) \quad \text{(A.11)}$$

APPENDIX B. SUPPLEMENTARY MATERIAL

Supplementary data to this article can be found online at https://doi.org/10.1016/j.gca.2018.11.037.

REFERENCES

Alkattan M., Oelkers E. H., Dandurand J.-L. and Schott J. (1998) An experimental study of calcite and limestone dissolution rates as a function of pH from -1 to 3 and temperature from 25 to 80 °C. *Chem. Geol.* **151**, 199–214.

Arakaki T. and Mucci A. (1995) A continuous and mechanistic representation of calcite reaction-controlled kinetics in dilute solutions at 25°C and 1 atm total pressure. *Aquat. Geochem.* **1**, 105–130.

Archer D. (1996) A data-driven model of the global calcite lysocline. *Global Biogeochem. Cycles* **10**, 511–526.

Archer D. E. (1991) Equatorial pacific calcite preservation cycles: production or dissolution? *Paleoceanography* **6**, 561–571.

Archer D., Eby M., Brovkin V., Ridgwell A., Cao L., Mikolajewicz U., Caldeira K., Matsumoto K., Munhoven G., Montenegro A. and Tokos K. (2009) Atmospheric lifetime of fossil fuel carbon dioxide. *Annu. Rev. Earth Planet. Sci.* **37**, 117–134.

Arvidson R. S., Collier M., Davis K. J., Vinson M. D., Amonette J. E. and Luttge A. (2006) Magnesium inhibition of calcite dissolution kinetics. *Geochim. Cosmochim. Acta* **70**, 583–594.

Arvidson R. S., Ertan I. E., Amonette J. E. and Luttge A. (2003) Variation in calcite dissolution rates: a fundamental problem? *Geochim. Cosmochim. Acta* **67**, 1623–1634.

Arvidson R. S. and Luttge A. (2010) Mineral dissolution kinetics as a function of distance from equilibrium - New experimental results. *Chem. Geol.* **269**, 79–88.

Berelson W. M., Balch W. M., Najjar R., Feely R. a., Sabine C. and Lee K. (2007) Relating estimates of CaCO3 production, export, and dissolution in the water column to measurements of CaCO3 rain into sediment traps and dissolution on the sea floor: a revised global carbonate budget. *Global Biogeochem. Cycles* **21**, 1–15.

Berelson W. M., Hammond D. E., McManus J. and Kilgore T. E. (1994) Dissolution kinetics of calcium-carbonate in equatorial pacific sediments. *Global Biogeochem. Cycles* **8**, 219–235.

Berner R. A. and Morse J. W. (1974) Dissolution kinetics of calcium carbonate in sea water IV. Theory of calcite dissolution. *Am. J. Sci.* **274**, 108–134.

Boudreau B. P. (2013) Carbonate dissolution rates at the deep ocean floor. *Geophys. Res. Lett.* **40**, 744–748.

Boudreau B. P. and Luo Y. (2017) Retrodiction of secular variations in deep-sea CaCO3 burial during the Cenozoic. *Earth Planet. Sci. Lett.* **474**, 1–12.

Buhmann D. D. W. (1987) Calcite dissolution kinetics in the system H2O-CO2-CaCO3 with participation of foreigns ions. *Chem. Geol.* **64**, 89–102.

Burton W. K. and Cabrera N. (1949) Crystal growth and surface structure. Part I. *Discuss. Faraday Soc.* **5**, 33.

Burton W. K., Cabrera N. and Frank F. C. (1951) The growth of crystals and the equilibrium structure of their surfaces. *Philos. Trans. Roy. Soc. A Math. Phys. Eng. Sci.* **243**, 299–358.

Busenberg E. and Plummer L. N. (1986) A comparative study of the dissolution and crystal growth kinetics of calcite and aragonite. *Stud. Diagenesis, U.S Geol. Surv. Bull.* **1578**, 139–168.

Byrne R. H., Mecking S., Feely R. A. and Liu X. (2010) Direct observations of basin-wide acidification of the North Pacific Ocean. *Geophys. Res. Lett.* **37**, n/a-n/a.

Cabrera N. and Levine M. M. (1956) XLV. On the dislocation theory of evaporation of crystals. *Philos. Mag.* **1**, 450–458.

Cabrera N., Levine M. M. and Plaskett J. S. (1954) Hollow dislocations and etch pits. *Phys. Rev.* **96**, 1153.

Chernov A. A. (1984) *Modern Crystallography III: Crystal Growth*. Springer Science & Business Media.

Chernov A. A., Rashkovich L. N. and Mkrtchan A. A. (1986) Solution growth kinetics and mechanism: prismatic face of ADP. *J. Cryst. Growth* **74**, 101–112.

Chou L., Garrels R. M. and Wollast R. (1989) Comparative study of the kinetics and mechanisms of dissolution of carbonate minerals. *Chem. Geol.* **78**, 269–282.

Cubillas P., Köhler S., Prieto M., Chaïrat C. and Oelkers E. H. (2005) Experimental determination of the dissolution rates of calcite, aragonite, and bivalves. *Chem. Geol.* **216**, 59–77.

Dickson A. G. and Millero F. J. (1987) A comparison of the equilibrium constants for the dissociation of carbonic acid in seawater media. 34, 1733–1743.

Dickson A. G., Wesolowski D. J., Palmer D. A. and Mesmer R. E. (1990) Dissociation constant of bisulfate ion in aqueous sodium chloride solutions to 250 °C. *J. Phys. Chem.* **94**, 7978–7985.

Dobberschütz S., Nielsen M. R., Sand K. K., Civioc R., Bovet N., Stipp S. L. S. and Andersson M. P. (2018) The mechanisms of crystal growth inhibition by organic and inorganic inhibitors. *Nat. Commun.* **9**, 1–6.

Doney S. C., Fabry V. J., Feely R. A. and Kleypas J. A. (2009) Ocean acidification: the other CO2 problem. *Ann. Rev. Mar. Sci.* **1**, 169–192.

Dong S., Subhas A. V., Rollins N. E., Naviaux J. D., Adkins J. F. and Berelson W. M. (2018) A kinetic pressure effect on calcite dissolution in seawater. *Geochim. Cosmochim. Acta* **238**, 411–423.

Dove P. M., Han N., Wallace A. F. and De Yoreo J. J. (2008) Kinetics of amorphous silica dissolution and the paradox of the silica polymorphs. *Proc. Natl. Acad. Sci. U. S. A.* **105**, 9903–9908.

Dove P. M., Han N. and Yoreo J. J. D (2005) Mechanisms of classical crystal growth theory explain quartz and silicate dissolution behavior. *Proc. Natl. Acad. Sci.* **102**, 10566.

Dunne J. P., Hales B. and Toggweiler J. R. (2012) Global calcite cycling constrained by sediment preservation controls. *Global Biogeochem. Cycles* **26**, 1–14.

Feely R. A., Sabine C. L., Byrne R. H., Millero F. J., Dickson A. G., Wanninkhof R., Murata A., Miller L. A. and Greeley D. (2012) Decadal changes in the aragonite and calcite saturation state of the Pacific Ocean. *Global Biogeochem. Cycles* **26**, 1–15.

Feely R. A., Sabine C. L., Lee K., Berelson W., Kleypas J., Fabry V. J. and Millero F. J. (2004) Impact of anthropogenic CO2 on the CaCO3 system in the oceans. *Science (80-.)* **305**, 362–366.

Finneran D. W. and Morse J. W. (2009) Calcite dissolution kinetics in saline waters. *Chem. Geol.* **268**, 137–146.

Fischer C., Arvidson R. S. and Lüttge A. (2012) How predictable are dissolution rates of crystalline material? *Geochim. Cosmochim. Acta* **98**, 177–185.

Fischer C., Kurganskaya I., Schäfer T. and Lüttge A. (2014) Variability of crystal surface reactivity: What do we know? *Appl. Geochem.* **43**, 132–157.

Fischer C. and Lüttge A. (2018) Pulsating dissolution of crystalline matter. *Proc. Natl. Acad. Sci.* **115**, 201711254.

Fukuhara T., Tanaka Y., Ioka N. and Nishimura A. (2008) An in situ experiment of calcium carbonate dissolution in the central Pacific Ocean. *Int. J. Greenh. Gas Control* **2**, 78–88.

Gehlen M., Bassinot F. C., Chou L. and McCorkle D. (2005) Reassessing the dissolution of marine carbonates: II. Reaction kinetics. *Deep Sea Res. Part I Oceanogr. Res. Pap.* **52**, 1461–1476.

De Giudici G. (2002) Surface control vs. diffusion control during calcite dissolution: Dependence of step-edge velocity upon solution pH. *Am. Mineral.* **87**, 1279–1285.

Gledhill D. K. and Morse J. W. (2006) Calcite dissolution kinetics in Na-Ca-Mg-Cl brines. *Geochim. Cosmochim. Acta* **70**, 5802–5813.

Gratz A. J., Hillner P. E. and Hansma P. K. (1993) Step dynamics and spiral growth on calcite. *Geochim. Cosmochim. Acta* **57**, 491–495.

Gutjahr A., Dabringhaus H. and Lacmann R. (1996) Studies of the growth and dissolution kinetics of the CaCO3 polymorphs calcite and aragonite.1. Growth and dissolution rates in water. *J. Cryst. Growth* **158**, 296–309.

Hales B. and Emerson S. (1997) Evidence in support of first-order dissolution kinetics of calcite in seawater. *Earth Planet. Sci. Lett.* **148**, 317–327.

Harstad A. O. and Stipp S. L. S. (2007) Calcite dissolution: effects of trace cations naturally present in Iceland spar calcites. *Geochim. Cosmochim. Acta* **71**, 56–70.

Honjo S. and Erez J. (1978) Dissolution rates of calcium carbonate in the deep ocean: an in situ experiment in the North Atlantic Ocean. *Earth Planet. Sci. Lett.* **40**, 287–300.

Ilyina T. and Zeebe R. E. (2012) Detection and projection of carbonate dissolution in the water column and deep-sea sediments due to ocean acidification. *Geophys. Res. Lett.* **39**, 1–6.

Jahnke R. A., Craven D. B. and Gaillard J.-F. (1994) The influence of organic matter diagenesis on CaCO3 dissolution at the deep-sea floor. *Geochim. Cosmochim. Acta* **58**, 2799–2809.

Jansen H., Zeebe R. E. and Wolf-Gladrow D. A. (2002) Modeling the dissolution of settling CaCO3 in the ocean. *Global Biogeochem. Cycles* **16**, 11–16.

de Kanel J. and Morse J. W. (1978) The chemistry of orthophosphate uptake from seawater on to calcite and aragonite. *Geochim. Cosmochim. Acta* **42**, 1335–1340.

Keir R. S. (1980) The dissolution kinetics of biogenic calcium carbonates in seawater. *Geochim. Cosmochim. Acta* **44**, 241–252.

Keir R. S. (1983) Variation in the carbonate reactivity of deep-sea sediments: determination from flux experiments. *Deep Sea Res. Part A. Oceanogr. Res. Pap.* **30**, 279–296.

Klasa J., Ruiz-Agudo E., Wang L. J., Putnis C. V., Valsami-Jones E., Menneken M. and Putnis A. (2013) An atomic force microscopy study of the dissolution of calcite in the presence of phosphate ions. *Geochim. Cosmochim. Acta* **117**, 115–128.

Koutsoukos P. G. and Kontoyannis C. G. (1984) Precipitation of calcium carbonate in aqueous solutions. *J. Chem. Soc Faraday Trans.* **1**, 1181–1192.

Lasaga A. C. (1998) *Kinetic Theory in the Earth Sciences*. Princeton University Press.

Lasaga A. C. and Lüttge A. (2001) Variation of crystal dissolution rate based on a dissolution stepwave model. *Science (80-.)* **291**, 2400–2404.

Lea A. S., Amonette J. E., Baer D. R., Liang Y. and Colton N. G. (2001) Microscopic effects of carbonate, manganese, and strontium ions on calcite dissolution. *Geochim. Cosmochim. Acta* **65**, 369–379.

Liang Y. and Baer D. R. (1997) Anisotropic dissolution at the CaCO3(104)—water interface. *Surf. Sci.* **373**, 275–287.

Liang Y., Baer D. R., McCoy J. M., Amonette J. E. and LaFemina J. P. (1996) Dissolution kinetics at the calcite-water interface. *Geochim. Cosmochim. Acta* **60**, 4883–4887.

Lüttge A. (2006) Crystal dissolution kinetics and Gibbs free energy. *J. Electron Spectros. Relat. Phenomena* **150**, 248–259.

MacInnis I. N. and Brantley S. L. (1992) The role of dislocations and surface morphology in calcite dissolution. *Geochim. Cosmochim. Acta* **56**, 1113–1126.

Malkin A. I., Chernov A. A. and Alexeev I. V. (1989) Growth of Dipyramidal face of dislocation-free ADP crystals; free energy of steps. *J. Cryst. Growth* **97**, 765–769.

Mehrbach C., Culberson C. H., Hawley J. E. and Pytkowicz R. M. (1973) Measurement of the apparent dissociation constants of carbonic acid in seawater at atmospheric pressure. *Limnol. Oceanogr.* **18**, 897–907.

Millero F., Huang F., Zhu X., Liu X. and Zhang J. (2001) Adsorption and desorption of phosphate on calcite and aragonite in seawater. *Aquat. Geochem.* **7**, 33–56.

Milliman J. D., Troy P. J., Balch W. M., Adams A. K., Li Y. H. and Mackenzie F. T. (1999) Biologically mediated dissolution of calcium carbonate above the chemical lysocline? *Deep Res. Part I Oceanogr. Res. Pap.* **46**, 1653–1669.

Morse J. W. (1978) Dissolution kinetics of calcium carbonate in sea water; VI, The near-equilibrium dissolution kinetics of calcium carbonate-rich deep sea sediments. *Am. J. Sci.* **278**, 344–353.

Morse J. W. and Arvidson R. S. (2002) The dissolution kinetics of major sedimentary carbonate minerals. *Earth-Sci. Rev.* **58**, 51–84.

Morse J. W., Arvidson R. S. and Lüttge A. (2007) Calcium carbonate formation and dissolution. *Chem. Rev.* **107**, 342–381.

Morse J. W. and Berner R. A. (1972) Dissolution kinetics of calcium carbonate in seawater: II. A kinetic origin for the lysocline. *Am. J. Sci.* **274**, 638–647.

Morse J. W. and Mackenzie F. T. (1990) Geochemistry of Sedimentary Carbonates. In Developments in Sedimentology 48 p. iii–x, 1–707.

Morse J. W., Wang Q. and Tsio M. Y. (1997) Influences of temperature and Mg:Ca ratio on CaCO3 precipitates from seawater. *Geology* **25**, 85–87.

Mucci A. (1986) Growth kinetics and composition of magnesian calcite overgrowths precipitated from seawater: Quantitative influence of orthophosphate ions. *Geochim. Cosmochim. Acta* **50**, 2255–2265.

Mucci A. and Morse J. W. (1983) The incorporation of Mg2+ and Sr2+ into calcite overgrowths: influences of growth rate and solution composition. *Geochim. Cosmochim. Acta* **47**, 217–233.

Mucci A. and Morse J. W. (1984) The solubility of calcite in seawater of various magnesium concentrations, I=0.697 m at 25°C and one atmosphere total pressure. *Geochim. Cosmochim. Acta* **48**, 815–822.

Olsen A., Key R. M., Van Heuven S., Lauvset S. K., Velo A., Lin X., Schirnick C., Kozyr A., Tanhua T., Hoppema M., Jutterström S., Steinfeldt R., Jeansson E., Ishii M., Pérez F. F. and Suzuki T. (2016) The global ocean data analysis project version 2 (GLODAPv2) – an internally consistent data product for the world ocean. *Earth Syst. Data Sci.* **8**, 297–323.

Peterson M. N. (1966) Calcite: rates of dissolution in a vertical profile in the central pacific. *Science (80-.)*. **154**, 1542–1544.

Plummer L. N., Parkhurst D. L. and Wigley T. M. L. (1979) Critical Review of the Kinetics of Calcite Dissolution and Precipitation. pp. 537–573.

Plummer L. N., Wigley T. M. L. and Parkhurst D. L. (1978) The kinetics of calcite dissolution in CO2-water systems at 5C to 60C and 0.0 to 1.0 atm CO2. *Am. J. Sci.* **278**, 179–216.

Pokrovsky O. S. (1998a) Precipitation of calcium and magnesium carbonates from homogeneous supersaturated solutions. *J. Cryst. Growth* **186**, 233–239.

Pokrovsky O. S. (1998b) Surface speciation of Ca and Mg carbonate minerals in aqueous solutions: a combined potentiometric, electrokinetic, and DRIFT surface spectroscopy approach. *Mineral. Mag.* **62A**, 1196–1197.

Pokrovsky O. S., Golubev S. V. and Schott J. (2005) Dissolution kinetics of calcite, dolomite and magnesite at 25°C and 0 to 50 atm pCO2. *Chem. Geol.* **217**, 239–255.

Pokrovsky O. S., Golubev S. V., Schott J. and Castillo A. (2009) Calcite, dolomite and magnesite dissolution kinetics in aqueous solutions at acid to circumneutral pH, 25 to 150°C and 1 to 55 atm pCO2: new constraints on CO2 sequestration in sedimentary basins. *Chem. Geol.* **260**, 317–329.

Pokrovsky O. S. and Schott J. (2002) Surface chemistry and dissolution kinetics of divalent metal carbonates. *Environ. Sci. Technol.* **36**, 426–432.

Rickard D. T. and Sjöberg E. L. (1983) Mixed kinetic control of calcite dissolution rates. *Am. J. Sci.* **283**, 815–830.

Ruiz-Agudo E. and Putnis C. V. (2012) Direct observations of mineral fluid reactions using atomic force microscopy: the specific example of calcite. *Mineral. Mag.* **76**, 227–253.

Ruiz-Agudo E., Putnis C. V., Jiménez-López C. and Rodriguez-Navarro C. (2009) An atomic force microscopy study of calcite dissolution in saline solutions: the role of magnesium ions. *Geochim. Cosmochim. Acta* **73**, 3201–3217.

Salem M. R., Mangood A. H. and Hamdona S. K. (1994) Dissolution of calcite crystals in the presence of some metal ions. *J. Mater. Sci.* **29**, 6463–6467.

Sand K. K., Tobler D. J., Dobberschütz S., Larsen K. K., Makovicky E., Andersson M. P., Wolthers M. and Stipp S. L. S. (2016) Calcite growth kinetics: dependence on saturation index, Ca2+:CO32-activity ratio, and surface atomic structure. *Cryst. Growth Des.* **16**, 3602–3612.

Schott J., Pokrovsky O. S. and Oelkers E. H. (2009) The link between mineral dissolution/precipitation kinetics and solution chemistry. *Rev. Mineral. Geochem.* **70**, 207–258.

Sjöberg E. L. (1978) Kinetics and mechanism of calcite dissolution in aqueous solutions at low temperatures. In Stockholm Contributions in Geology pp. 1–96.

Sjöberg E. L. and Rickard D. (1983) The influence of experimental design on the rate of calcite dissolution. *Geochim. Cosmochim. Acta* **47**, 2281–2285.

Sjöberg E. L. and Rickard D. T. (1984) Temperature dependence of calcite dissolution kinetics between 1 and 62°C at pH 2.7 to 8.4 in aqueous solutions. *Geochim. Cosmochim. Acta* **48**, 485–493.

Sjöberg E. L. and Rickard D. T. (1985) The effect of added dissolved calcium on calcite dissolution kinetics in aqueous solutions at 25°C. *Chem. Geol.* **49**, 405–413.

Song J., Zeng Y., Wang L., Duan X., Puerto M., Chapman W. G., Biswal S. L. and Hirasaki G. J. (2017) Surface complexation modeling of calcite zeta potential measurements in brines with mixed potential determining ions (Ca2+, CO32−, Mg2+, SO42−) for characterizing carbonate wettability. *J. Colloid Interface Sci.* **506**, 169–179.

Subhas A. V., Rollins N. E., Berelson W. M., Dong S., Erez J. and Adkins J. F. (2015) A novel determination of calcite dissolution kinetics in seawater. *Geochim. Cosmochim. Acta* **170**, 51–68.

Subhas A. V., Rollins N. E., Berelson W. M., Erez J., Ziveri P., Langer G. and Adkins J. F. (2018) The dissolution behavior of biogenic calcites in seawater and a possible role for magnesium and organic carbon. *Mar. Chem.* **205**, 100–112.

Subhas A. V., Adkins J. F., Rollins N. E., Naviaux J., Erez J. and Berelson W. M. (2017) Catalysis and chemical mechanisms of calcite dissolution in seawater. *Proc. Natl. Acad. Sci.* **114**, 8175–8180.

Sulpis O., Lix C., Mucci A. and Boudreau B. P. (2017) Calcite dissolution kinetics at the sediment-water interface in natural seawater. *Mar. Chem.* **195**, 70–83.

Svensson U. and Dreybrodt W. (1992) Dissolution kinetics of natural calcite minerals in CO2-water systems approaching calcite equilibrium. *Chem. Geol.* **100**, 129–145.

Teng H. H. (2004) Controls by saturation state on etch pit formation during calcite dissolution. *Geochim. Cosmochim. Acta* **68**, 253–262.

Uppström L. R. (1974) The boron/chlorinity ratio of deep-sea water from the Pacific Ocean. *Deep. Res. Oceanogr. Abstr.* **21**, 161–162.

Van Cappellen P., Charlet L., Stumm W. and Wersin P. (1993) A surface complexation model of the carbonate mineral-aqueous solution interface. *Geochim. Cosmochim. Acta* **57**, 3505–3518.

Vinson M. D. and Luttge A. (2005) Multiple length-scale kinetics: an integrated study of calcite dissolution rates and strontium inhibition. *Am. J. Sci.* **305**, 119–146.

Walter L. M. and Burton E. A. (1986) The effect of orthophosphate on carbonate mineral dissolution rates in seawater. *Chem. Geol.* **56**, 313–323.

Walter L. M. and Morse J. W. (1985) The dissolution kinetics of shallow marine carbonates in seawater: a laboratory study. *Geochim. Cosmochim. Acta* **49**, 1503–1513.

Wang X., Conway W., Burns R., McCann N. and Maeder M. (2010) Comprehensive study of the hydration and dehydration reactions of carbon dioxide in aqueous solution. *J. Phys. Chem. A* **114**, 1734–1740.

Wolthers M., Charlet L. and Van Cappellen P. (2008) The surface chemistry of divalent metal carbonate minerals: a critical assessment of surface charge and potential data using the charge distribution multi-site ion complexation model. *Am. J. Sci.* **308**, 905–941.

Wolthers M., Nehrke G., Gustafsson J. P. and Van Cappellen P. (2012) Calcite growth kinetics: modeling the effect of solution stoichiometry. *Geochim. Cosmochim. Acta* **77**, 121–134.

Xu J., Fan C. and Teng H. H. (2012) Calcite dissolution kinetics in view of Gibbs free energy, dislocation density, and pCO2. *Chem. Geol.* **322–323**, 11–18.

Xu M., Hu X., Knauss K. G. and Higgins S. R. (2010) Dissolution kinetics of calcite at 50–70°C: an atomic force microscopic study under near-equilibrium conditions. *Geochim. Cosmochim. Acta* **74**, 4285–4297.

Zhang J. and Nancollas G. H. (1992) Kinetics and mechanisms of octacalcium phosphate dissolution at 37C. *J. Phys. Chem* **96**, 5478–5483.

Zhong S. and Mucci A. (1989) Calcite and aragonite precipitation from seawater solutions of various salinities: precipitation rates and overgrowth compositions. *Chem. Geol.* **78**, 283–299.

Zuddas P. and Mucci A. (1998) Kinetics of calcite precipitation from seawater: II. The influence of the ionic strength. *Geochim. Cosmochim. Acta* **62**, 757–766.

Associate editor: Alfonso Mucci